Supplementary Information (SI) for Journal of Materials Chemistry A.

Electronic Supplementary Information

Room-temperature thermochemical water splitting: efficient mechanocatalytic hydrogen production

Takuya Yamamoto,[a] Sho Ashida,[b] Nanami Inubuse,[a] Shintaro Shimizu,[b] Yui Miura,[b] Tomoya Mizutani,[b] and Ken-ichi Saitow *[a,b,c]

[a] Department of Chemistry, Graduate School of Science, Hiroshima University; 1-3-1 Kagamiyama, Higashi-Hiroshima, Hiroshima 739-8526, Japan.

[b] Department of Chemistry, Graduate School of Advanced Science and Engineering, Hiroshima University; 1-3-1 Kagamiyama, Higashi-Hiroshima, Hiroshima 739-8526, Japan.

[c] Department of Materials Science, Natural Science Center for Basic Research and Development (N-BARD), Hiroshima University; 1-3-1 Kagamiyama, Higashi-Hiroshima, Hiroshima 739-8526, Japan.

*Corresponding author: Ken-ichi Saitow, saitow@hiroshima-u.ac.jp

Table of Contents

Note S1. H_2 amount calculations and gaseous reaction products

H_2 amount calculations

The temperature and pressure of the gas in the milling vessel were tracked *in situ* during milling, with measurements acquired every second. Using the measured pressure $P(T, t)$ and temperature T of the gas at milling time t, the water vapor pressure $P_{H_2O}(T, t)$, the Ar partial pressure $P_{Ar}(T, t)$, and the equation of state for an ideal gas, the amount of H_2 was quantified:

$$P_{H_2}(T,t) = P(T,t) - P_{H_2O}(T,t) - P_{Ar}(T,t) \tag{S1}$$

$P_{H_2O}(T,t)$ was determined from T measured at milling time t and the Tetens equation[1]:

$$P_{H_2O}(T,t) = 6.1078 \times 10^{\frac{7.5(T-273.1)}{((T-273.1)+237.3)}} \tag{S2}$$

$P_{Ar}(T, t)$ was determined for the use of Ar as the ambient gas when the vessel containing the metal was placed in a glove box:

$$P_{Ar}(T,t) = \frac{n_{Ar}RT}{V} \tag{S3}$$

$$n_{Ar} = \frac{P_{Ar}V}{RT_{lab}} \tag{S4}$$

where n_{Ar} is the molar amount of Ar, R is the molar gas constant, V is the volume of the vessel (52.8 mL), P_{Ar} is the pressure of Ar in the glove box (0.101 MPa), and T_{lab} is the temperature of the laboratory (296.3 K). The amount of H_2 was calculated according to $P_{H_2}(T, t)$ using

$$n_{H_2} = \frac{P_{H_2}(T,t)V}{RT} \tag{S5}$$

Gas content of the vessel

Fig. S1 shows typical results for the analysis of the gas content in the milling vessel during the mechanochemical Ti–water reactions. The data shown corresponds to that presented for the Ti–water reaction in Fig. 1C. Each gas pressure value was obtained from *in situ* measurements of the total pressure $P(T, t)$ and temperature $T(t)$ in the milling vessel, using Eqn (S1)–(S3), as described above.

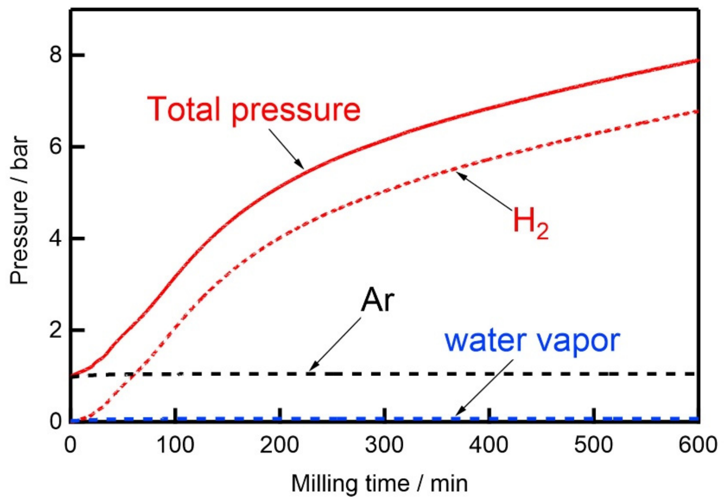

Fig. S1. Gas content of the vessel. The data shown corresponds to that shown for the mechanochemical Ti–water reaction in Fig. 1C.

Note S2. Gas chromatography of mechanochemical metal–water reactions

Fig. S2 shows a schematic diagram of the gas collection system. This system was purpose-built to analyze the gas generated by the mechanochemical metal–water reactions. The system consists of a gas sampling bag (GL science, smart bag PA CEK-0.1), vacuum pump, valves, and stainless-steel tubes. The measurement procedure is now described. First, the air in the tubes and the sampling bag is evacuated by the vacuum pump. Second, the generated gas in the milling vessel is released into the bag. Third, a 100-µL gas volume is collected using a microsyringe and injected into a gas chromatography (GC) instrument (SHIMADZU, GC-2014). The GC instrument is equipped with a thermal conductivity detector (TCD) and used with either high-purity Ar or He as the carrier gas. A packed column (SHINCARBON ST, 2 m length, 3 mm diameter) is used, and the column flow rate is set to 30 mL min^{-1}. The column temperature is set to 40 °C and the vaporizer/detector temperature to 120 °C (for Ar) or 100 °C (for He).

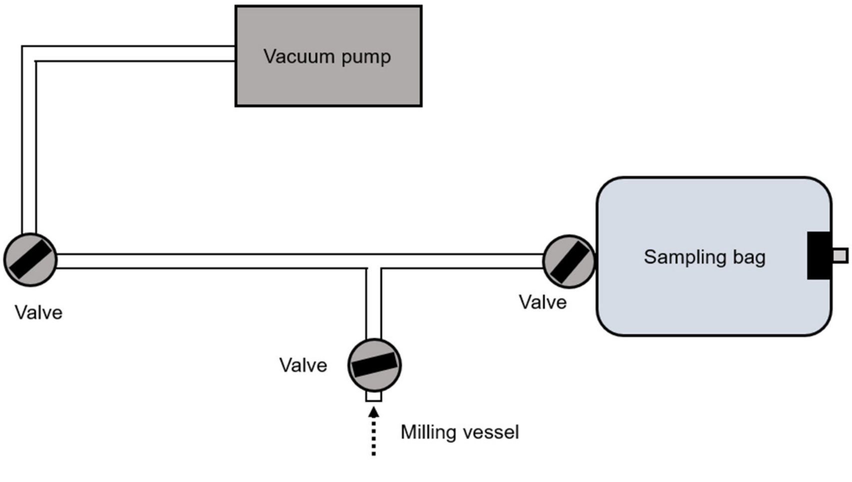

Fig. S2. Schematic diagram of the gas collection system. The system was designed and constructed specifically for the purpose of gas chromatographic analysis of the gases generated during the mechanochemical metal–water reactions.

Ar and He carrier gases were chosen for the analysis of H_2 and the other gases, respectively. This is because the TCD offers a high signal-to-noise ratio when the difference in the thermal conductivities of the sample and carrier gas is large. We considered all of the gases that might possibly have been produced by the mechanochemical metal–water reactions with milling media made of either tungsten carbide (WC), stainless steel (SUS), or ZrO_2; the retention times of these gases—H_2, O_2, N_2, CH_4, CO_2, and CO—are listed in Table S1.

The use of He as the carrier gas allows the detection of polyatomic molecules (i.e., CO, CO_2, and CH_4) with high sensitivity, but the sensitivity of H_2 detection with this carrier gas is low. In contrast, the use of Ar as a carrier gas allows the detection of H_2 with high sensitivity and polyatomic molecules (i.e., CO, CO_2, and CH_4) with low sensitivity; the different GC sensitivities are listed in Table S2.

To quantify the gas concentrations, we prepared a calibration curve, using the linear relationship between the gas concentration and signal intensity, for six standard gases: H_2, O_2, N_2, CH_4, CO_2, and CO. As a result, we verified the purity of the generated gas as >99% H_2. In addition, small amounts of O_2 and N_2 (air contamination) were observed, but CO_2 and CO were not observed, and the CH_4 gas concentration was <0.8% (Fig. S3).

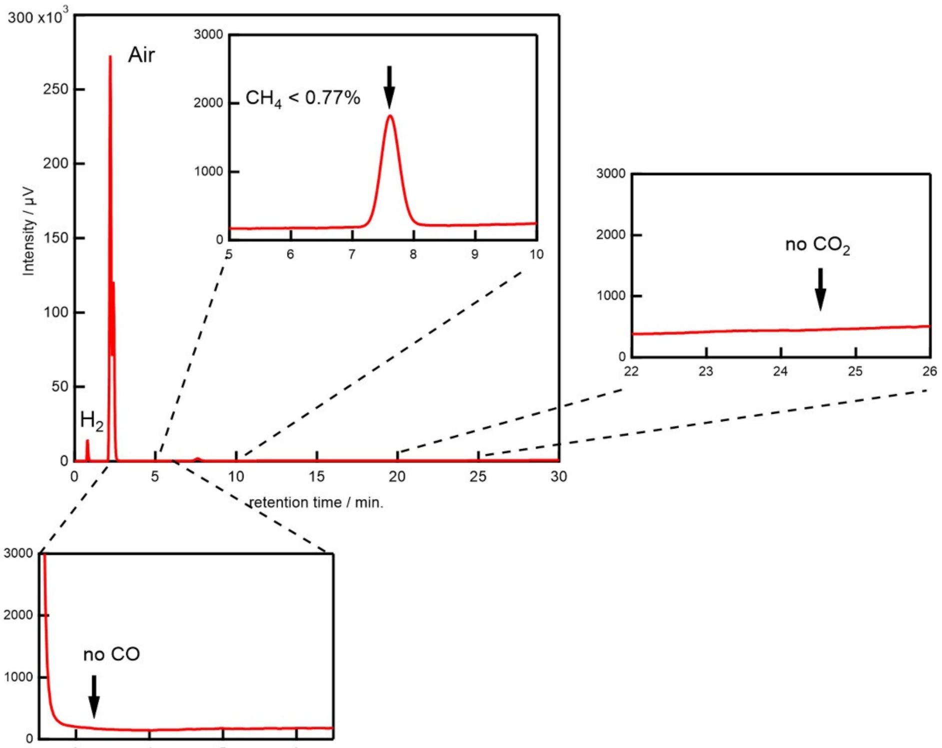

Fig. S3. GC data for gas generated by the mechanochemical Ti–water reaction. We carefully checked the signal for all the possible minor gases that might exist in the reaction vessel; He was used as the carrier gas to facilitate their detection. A small amount of CH_4 (<0.8%) and no CO_2 or CO were detected. The GC experiments were conducted using the WC milling medium, with 3.5 h of milling at 400 rpm.

Note S3. Induction period in mechanochemical reactions of Al and Zn systems

The H_2 production vs. time profiles of the mechanochemical reactions between water and Al or Zn include inflection points (Fig. 1E and F). This feature, observed only for the Al and Zn systems, was attributed to a so-called induction period[2]: the H_2 production rate was initially slow, and it gradually accelerated with time during the reaction, with the inflection point appearing subsequently, at the time when almost all the reactant metal placed in the vessel had been consumed by the reaction. In contrast, the other metals had H_2 production rates that were initially high and gradually decreased with time as the reactant metal was consumed. The induction period (induction time) is a well-established and important concept in H_2 production and has been frequently observed for many metal–water reactions.[2] Specifically, the H_2 production rate at the initial reaction stage is slow because the surface of the metal is covered by a passivation layer. In order to minimize the induction period, researchers have performed various pretreatments, such as the use of additives or alkaline solutions, increasing the surface area via particle size reduction, and alloy formation.[2–6] However, the mechanochemical metal–water reaction in the present study did not require any pretreatments owing the fact that mechanical milling and the reaction occurred simultaneously (Fig. 1E and F). In contrast, it is well-known that for Al and Zn, a passivation layer is easily formed, and a particularly long induction time is seen in reactions involving Al.[2] Moreover, since Al and Zn are soft metals with high ductility, cracks and defects, which promote the reaction with water, are not produced in large numbers during mechanical milling. As a result, in the Al and Zn systems, H_2 production was hindered even during mechanical milling with water; thus, these reactions were delayed, and hence long induction periods were observed (Fig. 1E and F).

Note S4. H_2 production and products of other metal–water reactions

The H_2 production yields of all the metals investigated in the present study are listed in Table 1. As shown in Fig. 1F, for Ti, extraordinary H_2 production occurred, unlike the other metals, for which the H_2 production yields were in the range of 20–100%. It should be emphasized that under standard-state conditions [i.e., 25 °C and 10^5 Pa (1 atm)], none of the hydrogen-producing metal–water reactions we examined in this study proceed easily because the passivation layer on the metal surfaces significantly hinders the reaction with water, and hence the resultant H_2 production is negligible. Therefore, to generate H_2 by reacting metals with water, metal pretreatments (additives, alkaline solutions, increasing the surface area via particle size reduction, alloy formation, and so on) are usually required.[2–6] However, the mechanochemical reactions in the present study efficiently produced H_2 from water without any pretreatment. This is because the milling process and reaction occurred simultaneously in water, destroying the passivation layer and increasing the surface area of the metal; this allowed the reaction to proceed in localized regions of high temperature T and pressure p at the sites of impact between colliding milling balls. Thus, the main focus of our study was the mechanochemical reaction between Ti species and water. However, with the aim of obtaining a clearer understanding of this specific mechanochemical metal–water reaction and its H_2 production, the other mechanochemical metal–water reactions were analyzed. Brief overviews of the results for the reaction of each metal are now presented.

Al system

Al does not easily react with water under standard-state conditions because a passivation layer is immediately formed on the Al surface, which prevents the reactants from accessing the metal surface.[2–6] However, the hydrogen-producing reaction between Al and water is the most well-studied system among the metal–water systems covered in the present study, and several review articles on this topic, including the exploration of the use of additives and/or alkaline water and alloying to promote the reaction, have been published.[3,5,6] Based on these studies, the overall reaction can be described in terms of the three reaction processes [Eqn (S6)–(S8)][2,3]:

$$Al + 3\ H_2O \rightarrow Al(OH)_3 + 3/2\ H_2 \qquad (S6)$$

$$Al + 2\ H_2O \rightarrow AlO(OH) + 3/2\ H_2 \qquad (S7)$$

$$Al + 3/2\ H_2O \rightarrow 1/2\ Al_2O_3 + 3/2\ H_2 \qquad (S8)$$

The results of DFT calculations indicate that the stabilities of the different forms of aluminum oxides and hydroxides are dependent on temperature T, with $Al(OH)_3$, $AlO(OH)$, and Al_2O_3 being formed at $T < 280$ °C, 280 °C $< T < 480$ °C, and $T > 480$ °C, respectively.[7] Note that all the reactions in Eqn (S6)–(S8) generate the same amount of H_2 using the same amount of Al. In the present study, we measured the XRD patterns of the solid products of the mechanochemical Al–water reactions performed using a revolution velocity of 400 rpm. For the Al system, the XRD pattern is shown in Fig. S4A, and the peaks in the pattern were assigned to three species. Since the diffraction pattern was dominated by the $Al(OH)_3$ peaks, we conclude that the reaction in Eqn (S6) was dominant, and hence this reaction was listed along with the other metal–water reactions in Table 1. However, Fig. S4A also demonstrates that three species were formed as solid reaction products. This indicates that the mechanochemical Al–water reactions proceed at local temperatures of ~480 °C. In addition, in this study, the mechanochemical reactions occurred in a high-energy ball mill, and local temperatures and pressures during collision impact between milling balls were calculated to be in the ranges of 300–1000 °C and 2–12 GPa, respectively, at revolution velocities of 100–800 rpm (Fig. 4A and B). The experimental XRD results and theoretical calculations revealed that the mechanochemical Al–water reaction proceeded at a high temperature (~480 °C) and pressure (>2 GPa). This thermodynamic state corresponds to supercritical water ($T_c = 374$ °C, $P_c = 22.1$ MPa), and hence we conclude that this exists at the sites of impact between milling balls.

Zn system

Zinc does not easily react with water at room temperature owing to the formation of a surface passivation layer, and small amounts of H_2 are produced by reacting this metal with warm water [Eqn (S9)].

$$Zn + 2H_2O \rightarrow Zn(OH)_2 + H_2 \qquad \text{in warm water} \qquad (S9)$$

$$Zn + H_2O \rightarrow ZnO + H_2 \qquad >250\ °C \qquad (S10)$$

Thus, there are very few papers reporting research into H_2 production as a result of the reaction between zinc and water.[8] However, many valuable studies have been conducted on H_2 production via Zn hydrolysis, i.e., the reaction between Zn and steam. This reaction requires harsh conditions, which can be realized via solar thermochemical processing.[8–11] Specifically, a slow reaction between Zn and steam occurs at temperatures of >250 °C. The reaction rate increases sharply above 400 °C, and the reaction proceeds vigorously, causing the release of additional exothermic heat from the powdered reactant.[8] In addition, there have been many reports of H_2 production via solar thermochemical water splitting in a Zn/ZnO system; at high temperatures (>1700 °C) and under dry conditions, ZnO is decomposed into Zn and O_2, efficiently reacting with steam [Eqn (S10)] at a temperature of ~700 °C to produce H_2.[9–11] Thus, Zn can be used to produce H_2 at high temperatures (>400 °C).

In the present study, we performed XRD on the solid products of the mechanochemical Zn–water reactions, and the resulting ZnO diffraction patterns are shown in Fig. S4B. Thus, it was confirmed that Eqn (S10) proceeded in the mechanochemical vessel, and hence this reaction was listed among the metal–water reactions in Table 1. In addition, the mechanochemical reactions occurred in a high-energy ball mill, and local temperatures and pressures during collisions between milling balls, at the sites of impact, were calculated to be in the ranges of 300–1000 °C and 2–12 GPa, respectively, at revolution velocities of 100–800 rpm (Fig. 4A and B). Based on the experimental XRD results and theoretical calculations, we conclude that the mechanochemical Zn–water reaction proceeded at a high temperature (>400 °C) and pressure (>2 GPa). These thermodynamic conditions at the collision impact sites between milling balls correspond to water existing in a supercritical state (T_c = 374 °C, P_c = 22.1 MPa).

Fe system

The steam–iron process is one of the oldest methods for producing H_2, and the reaction is a cyclic redox process in which coal and water are typically used as the reagents.[12] In addition, it is well-known that iron reacts vigorously with steam at high temperatures, with the formation of iron oxide and H_2 [Eqn (S11)].[12,13]

$$Fe + 4/3\ H_2O \rightarrow 1/3\ Fe_3O_4 + 4/3\ H_2 \qquad \text{in steam} \qquad (S11)$$

According to a thermodynamic study, this reaction proceeds at temperatures of >157 °C.[12] The same reaction has also been used to explain H_2 production via thermochemical water splitting or steam–iron processes at high temperatures.[12]

In the present study, we acquired the XRD pattern of the solid products of the mechanochemical Fe–water reactions, and Fe_3O_4 diffraction peaks were observed (Fig. S4C). Thus, the reaction in Eqn (S11) was listed in Table 1 among the metal–water reactions, and we can also conclude that, like the above-discussed Al–water and Zn–water reactions, the mechanochemical Fe–water reaction proceeded in localized high-temperature regions at the sites of impact between milling balls.

Mn system

An inorganic chemistry textbook[14] states that "Manganese reacts with warm water to give $Mn(OH)_2$ and H_2." Another inorganic chemistry textbook[13] explains that "Mn is more reactive than its neighbors in the periodic table. It reacts slowly with H_2O, liberating H_2." However, there are very few mentions in the literature of H_2 production as a result of the reaction between Mn and water and/or steam. Specifically, only a single paper reporting H_2 production owing to the reaction of Mn with water[15] has been published, to the best of our knowledge. According to the authors of that study, Mn efficiently generates H_2 when reacted with steam at 200 °C and 2.0 MPa, but the chemical equation of the reaction is not given.

In contrast, several thermochemical studies on H_2 production using manganese oxides, rather than metallic manganese, have been published. In these experiments, H_2 was generated by cyclic reactions between water and manganese oxides (i.e., Mn_2O_3/MnO, Mn_3O_4/MnO) in the presence of Na_2CO_3 or NaOH.[10,16] However, as far as we are aware, there have been no reports published on thermal water splitting using metallic manganese.

Based on the thermodynamic equilibrium of manganese oxides in an inert gas environment, it can be concluded that different manganese oxides are formed at different temperatures: MnO_2, Mn_2O_3, Mn_3O_4, and MnO are formed at 500–900, 500–1500, 500–1600, and 700–1900 °C, respectively.[16] Assuming these products are generated by reactions with steam at high temperature, the details of the reactions are as follows:

$Mn + 2\,H_2O \rightarrow MnO_2 + 2H_2$ in steam (S12)

$Mn + 3/2\,H_2O \rightarrow 1/2\,Mn_2O_3 + 3/2\,H_2$ in steam (S13)

$Mn + 4/3\,H_2O \rightarrow 1/3\,Mn_3O_4 + 4/3\,H_2$ in steam (S14)

$Mn + H_2O \rightarrow MnO + H_2$ in steam (S15)

XRD patterns of the solid products of the mechanochemical Mn–water reactions were obtained, and diffraction peaks were assigned to Mn_3O_4 (β-Mn_3O_4) and MnO_2 (λ-MnO_2) (Fig. S4D). The former is a commonly occurring phase, for which there is an abundance of electrochemical redox data, whereas the latter phase is rare, and its electrochemistry is not well characterized. In addition, it has been reported that Mn_3O_4 is thermodynamically 2–5 times more stable than MnO_2 at high temperatures (500–1300 °C).[16] By considering the observed XRD pattern and literature thermodynamic data, we concluded that the reaction producing Mn_3O_4 [Eqn (S14)] was the principal reaction occurring in the ball mill, and hence this was listed in Table 1 among the metal–water reactions. However, considering the temperature at which Mn_3O_4 and MnO_2 are formed (500–1600 °C)[16] and the calculated local temperature range (Fig. 4B), as well as the XRD results, it is clear that MnO_2 was formed, alongside Mn_3O_4, in the milling vessel. In conclusion, the mechanochemical Mn–water reaction also proceeded in localized high-temperature regions at the sites of impact between milling balls.

Sn system

There are very few mentions in the literature of H_2 production as a result of the reaction between Sn and water. One textbook states: "Tin is unaffected by water, and it reacts with steam to give tin dioxide and hydrogen" [Eqn (S17)].[13]

$$Sn + H_2O \rightarrow SnO + H_2 \qquad \text{in steam} \qquad (S16)$$

$$Sn + 2H_2O \rightarrow SnO_2 + 2H_2 \qquad \text{in steam} \qquad (S17)$$

However, there are several reports of H_2 production via thermochemical water splitting using this metal. Namely, a SnO_2/SnO thermochemical cycle with steam produced H_2 at a temperature of >350 °C [Eqn (S16) and (S17)], and the branching ratios changed with the heating temperature.[17,18]

In the present study, among all the metal–water reactions studied, the mechanochemical Sn–water reactions produced the smallest amount of H_2 (Fig. 4B). We acquired XRD measurements of the solid products of the mechanochemical Sn–water reactions (Fig. S4E), but almost all the diffraction peaks were assigned to Sn. This is because the thermochemical Sn–water reaction is inefficient, as concluded by the authors of a previous study.[15] Specifically, the reaction between Sn and steam generating H_2 is less reactive than that involving Al at 200 °C, producing a gas amount 30 times lower. One reason for this low H_2 production yield could be the low standard Gibbs energy for the reaction (Fig. 2D).

Sample preparation procedures for XRD measurements

After the mechanochemical reactions, the slurries in the vessel were collected by centrifugation at 7830 rpm for 20 min (Centrifuge 5430, Eppendorf), and the obtained precipitates were dried at 35 °C overnight before the XRD measurements were acquired with Cu K_α radiation (40 kV, 50 mA; SmartLab SE, Rigaku, Japan). For these measurements, a sample-holder plate made from nonreflecting silicon, custom-designed to guarantee a background-free signal, was used.

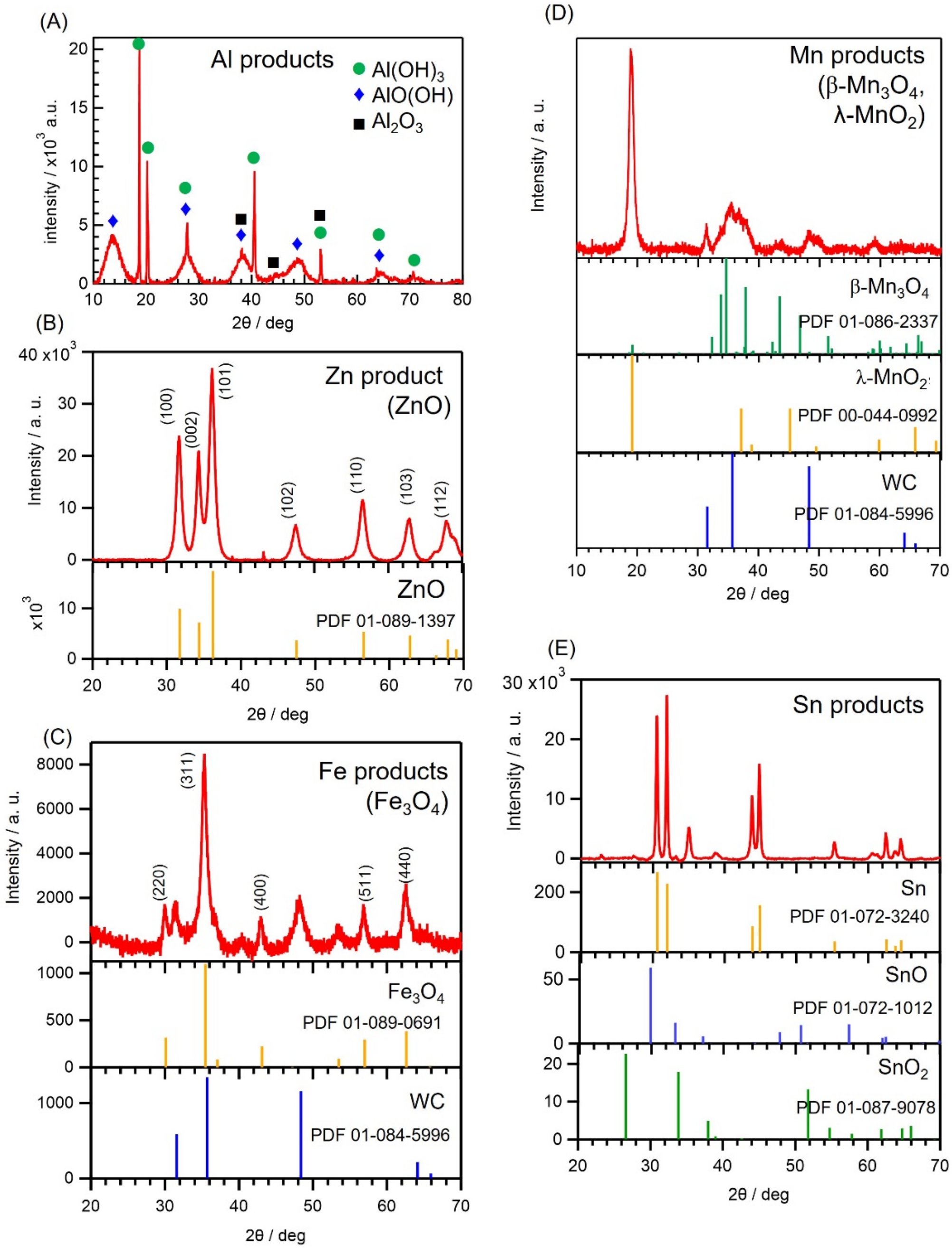

Fig. S4. XRD patterns of products of the mechanochemical metal–water reactions. Patterns for the products of the reactions between water and **A** Al, **B** Zn, **C** Fe, **D** Mn, and **E** Sn. The reagents were 4 mmol of Al, Fe, Mn, or Sn, or 2 mmol of Zn, and 10 mL of distilled water. The mechanochemical Al–water and Zn–water reactions were performed using the SUS milling medium, and the other reactions were performed using the WC milling medium. In each case except for the reaction with Sn, the revolution velocity was 400 rpm and the reaction time was 60 min; for the mechanochemical Sn–water reaction, which was less efficient, the reaction time was extended to 900 min. After the mechanochemical reaction, the obtained slurry was centrifuged. The dried powder was used as a sample for the XRD measurement with Cu K$_\alpha$ radiation. The bar XRD patterns of the standard materials were generated using powder diffraction data from the International Centre for Diffraction Data (ICDD) database, and the numbers embedded in each data indicate the ICCD PDF of their crystal structures.

Note S5. Mechanochemical reactions between tungsten or WC and water

We verified that H_2 is produced by the mechanochemical reaction between tungsten (W) and water (Fig. S5). In addition, to observe H_2 production owing to the reaction between the milling media (WC) and water, we performed milling with only the WC balls and water in the WC vessel, as shown in Fig. S6. The amounts of H_2 produced in the former and latter cases were small (13% and 7%, respectively, of that produced by the Ti–water reaction). Thus, it was verified that W-based materials were not directly responsible for the extraordinary amount of H_2 produced by the Ti–water reaction (Fig. 1E). Moreover, the amount of H_2 produced when the SUS milling balls and water, without any other reactant, were subjected to the mechanical treatment in the SUS vessel (black line in Fig. S6) was even smaller; it was 35 times lower than the amount of H_2 produced in the presence of Ti [compare Fig. S6 (0.4 mmol) and Fig. 1E (14 mmol) at 600 min]. To facilitate comparison, the ranges of the vertical axes in Fig. S5 and S6 are the same as those used for the right vertical axis of Fig. 1E.

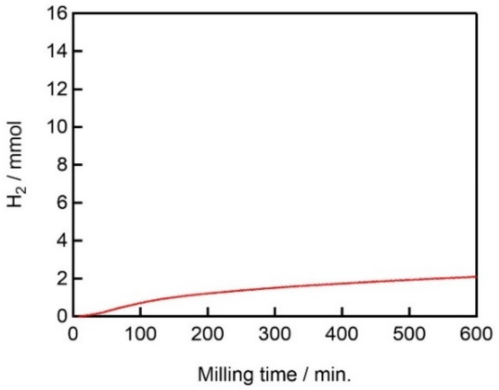

Fig. S5. H_2 production during the mechanochemical reactions between W and water. The milling medium was WC, and the revolution velocity was 400 rpm.

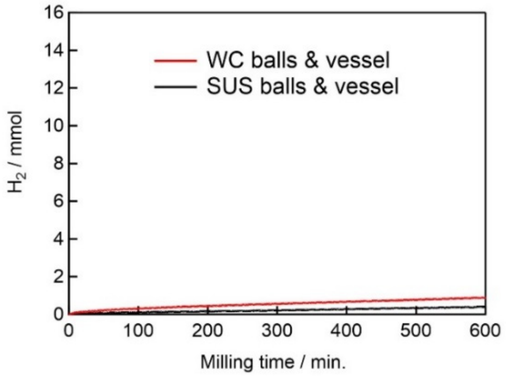

Fig. S6. H_2 production during the mechanochemical reactions between the milling media and water. This data can be considered background signals for H_2 production reactions performed using each specific milling medium. The revolution velocity was 400 rpm.

Note S6. Repeatability of the extraordinary H_2 production

To evaluate the repeatability of the extraordinary H_2 production of the mechanochemical Ti–water reactions, we repeated the reaction, and it was verified that the differences in the H_2 yields of the different repeats was <10%. In addition, when different graduate students conducted mechanochemical Ti–water reactions at different times over the course of several years, the resulting data were always similar, with extraordinary H_2 production being observed on each occasion. Several of these results are displayed in Fig. S7.

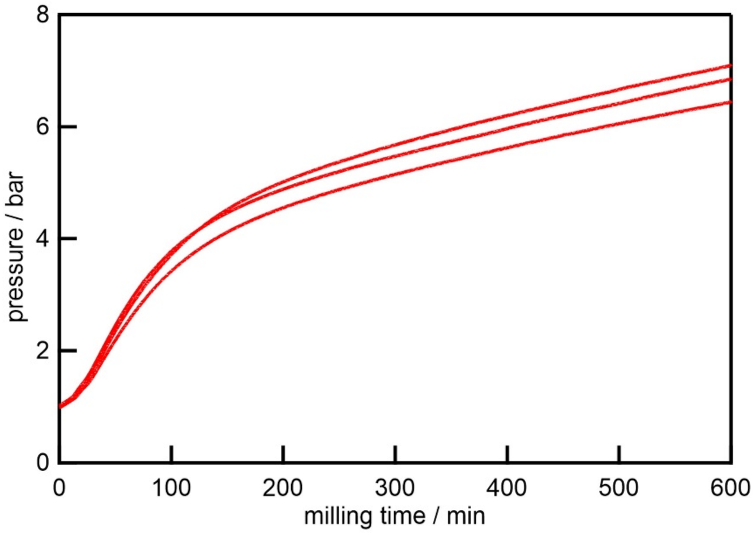

Fig. S7. Verification of the repeatability of the mechanochemical Ti–water reactions.

Note S7. Gas chromatogram of the mechanochemical TiO_2–water reaction products

Fig. S8 shows the GC data for the gas generated by the reaction between TiO_2 and water using the WC milling medium. A small amount of CH_4 was observed (<1%), but CO_2 and CO were not detected. For this measurement, He gas was used as the carrier gas because polyatomic molecules can be detected with high sensitivity using this gas, as explained above (Note S2).

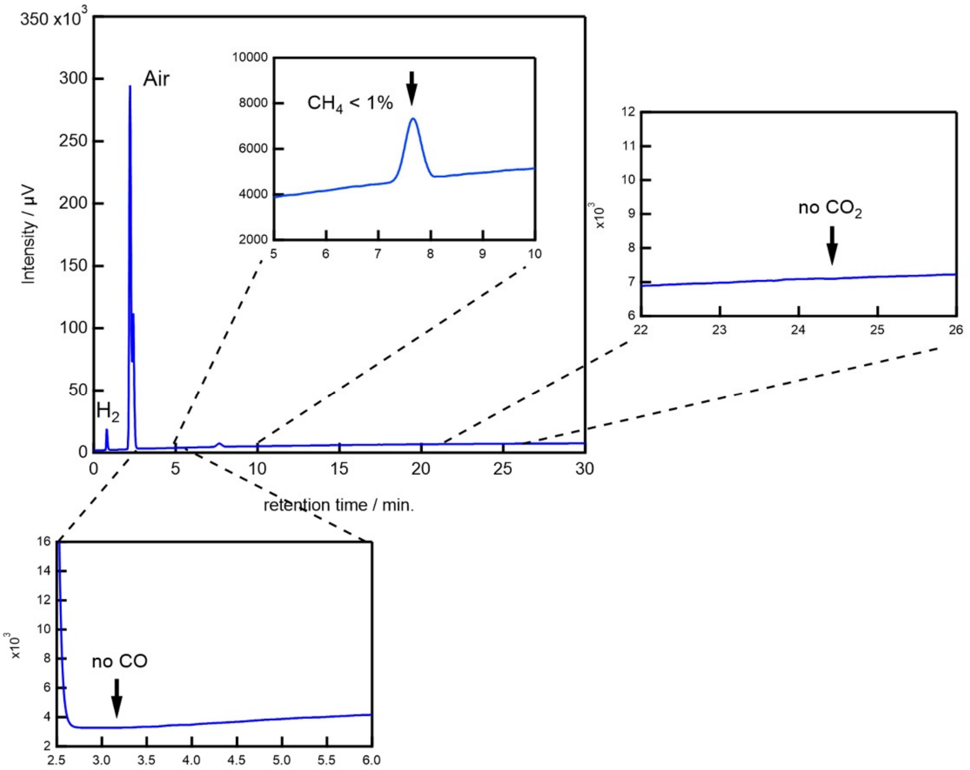

Fig. S8. GC data for the gases generated by the mechanochemical TiO_2–water reaction. Using He as the carrier gas, a small amount of CH_4 (<1%), and no CO_2 or CO, was detected. The mechanochemical reactions in this case were conducted using the WC milling medium with water at 400 rpm after 10 h of milling.

Note S8. H_2 production characteristics of the mechanochemical Ti–seawater reactions

The H_2 production behaviors of the mechanochemical reactions between Ti and distilled water or seawater did not differ significantly (Fig. 1J). Similar behavior was observed for the reactions between Mg and various aqueous salt solutions, with differences in this case being attributed to the properties of the salts.[19] Specifically, the H_2 production behaviors of the reactions between Mg and distilled water, aqueous NaCl, or aqueous KCl were found to be very similar. However, the amounts of H_2 produced by the reactions between Mg and either aqueous $MnCl_2$, aqueous $NiCl_2$, or aqueous $AlCl_3$ were 5, 7, and 8 times greater, respectively, than that produced by the Mg–distilled water reaction.[19] These differences were attributed to the ability of the cation species of each salt to hinder the formation of a passivation layer. As this idea is very interesting, a detailed investigation to test the hypothesis in the near future would be valuable.

Cl Analyses during mechanochemical Ti–seawater reactions

To investigate the fate of the salts in the seawater during the mechanochemical Ti–seawater reaction, we monitored the amount of Cl^- in the aqueous NaCl as a function of milling time. Aliquots of the solution (1 mL) were taken from the milling vessel at intervals during the mechanochemical reaction, and the amount of Cl^- in the solution was quantified via conventional titration, using 0.01 M aqueous $AgNO_3$, with AgCl being observed as a white precipitate. The color change to red of an indicator reagent (K_2CrO_4, 5 wt.%) was used to quantify the total amount of Cl^- in the sample solution with the formation of Ag_2CrO_4. The obtained results are shown in Fig. S9. The blue and gray lines represent the Cl^- concentrations measured in the titration experiments and calculated Cl^- concentrations, obtained for the use of seawater for H_2 production, respectively. The experimental data are in good agreement with the calculated data. In addition, no decrease in the Cl^- concentration was observed. Therefore, we can conclude that chlorine remained in the solution in the vessel as Cl^-, and Cl_2 gas was not emitted as a result of the mechanochemical Ti–seawater reaction.

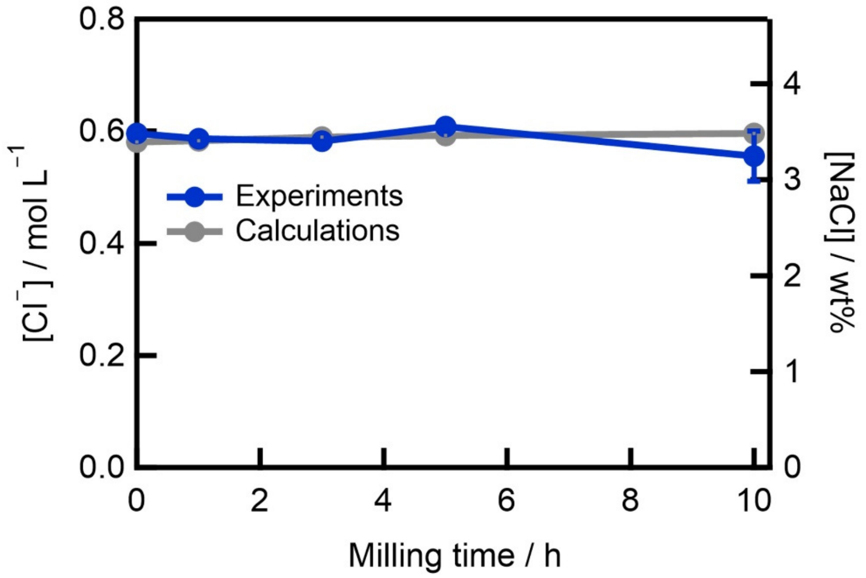

Fig. S9. Cl analyses during mechanochemical Ti–seawater reactions. The Cl^- and NaCl concentrations were obtained from titration measurements and calculations, respectively, as functions of the milling time. The error bars represent the standard deviations of three measurements acquired at each time during the reaction (milling time).

Next, we measured the FTIR spectra of the solid products of the Ti–water reaction to determine whether or not $TiCl_x$ products were formed. In addition, we compared these results with the FTIR spectra of the solid products of the mechanochemical Ti–seawater and Ti–distilled water reactions performed under the same milling conditions. The motivation for this comparison was to understand the fate of the salts present in the seawater during the mechanochemical Ti–seawater reaction from the viewpoint of solid products. The experimental procedures are described in the next paragraph. Fig. S10 shows the FTIR spectra of the solid products of 1-, 3-, and 5-h mechanochemical Ti–seawater and Ti–distilled water reactions (red lines). These results indicate that the solid products consisted of titanium oxide (TiO_2) and WO_3 mixtures. Thus, it was verified that mechanochemical Ti/TiO_x–distilled water and Ti/TiO_x–seawater reactions produced TiO_2 and WO_3 via catalytic cycles. In addition, note that a strong, narrow FTIR band at approximately 500 cm^{-1} is characteristic of $TiCl_x$,[20,21] but this signal was not observed in our spectra. Moreover, the FTIR spectra of the mechanochemical Ti–seawater reaction products were in good agreement with those of the mechanochemical Ti–distilled water reaction products. Therefore, $TiCl_x$ ($x = 1$–4) compounds were not formed in the present experiments. This is unsurprising, given that $TiCl_x$ is known to be unstable, immediately decomposing by reacting with moisture in the air; hence, its coexistence with water in the milling vessel is improbable.

Sample preparation procedures for FTIR measurements

FTIR absorption spectroscopy (FT/IR-4200, JASCO, Japan) was used to measure the IR spectra of the samples and several standards. To prepare the samples for these measurements, after the mechanochemical reactions, the slurries in the vessel were collected by centrifugation (Centrifuge 5430, Eppendorf) at 7830 rpm for 20 min, and the obtained precipitates were dried in preparation for the FTIR measurements. Since the measurements were conducted using the diffuse reflectance method, the dried precipitates were ground with KBr powder using a mortar and pestle. Each IR spectrum was measured three times to obtain averaged spectral data (Fig. S10). As reference data, we measured the FTIR spectra of Ti, TiO_2, Ti_2O_3, TiO, WC, and WO_3 powders, all of which were used as received. Thus, these standard FTIR spectra were used to characterize the solid products of the mechanochemical Ti–seawater and Ti–distilled water reactions.

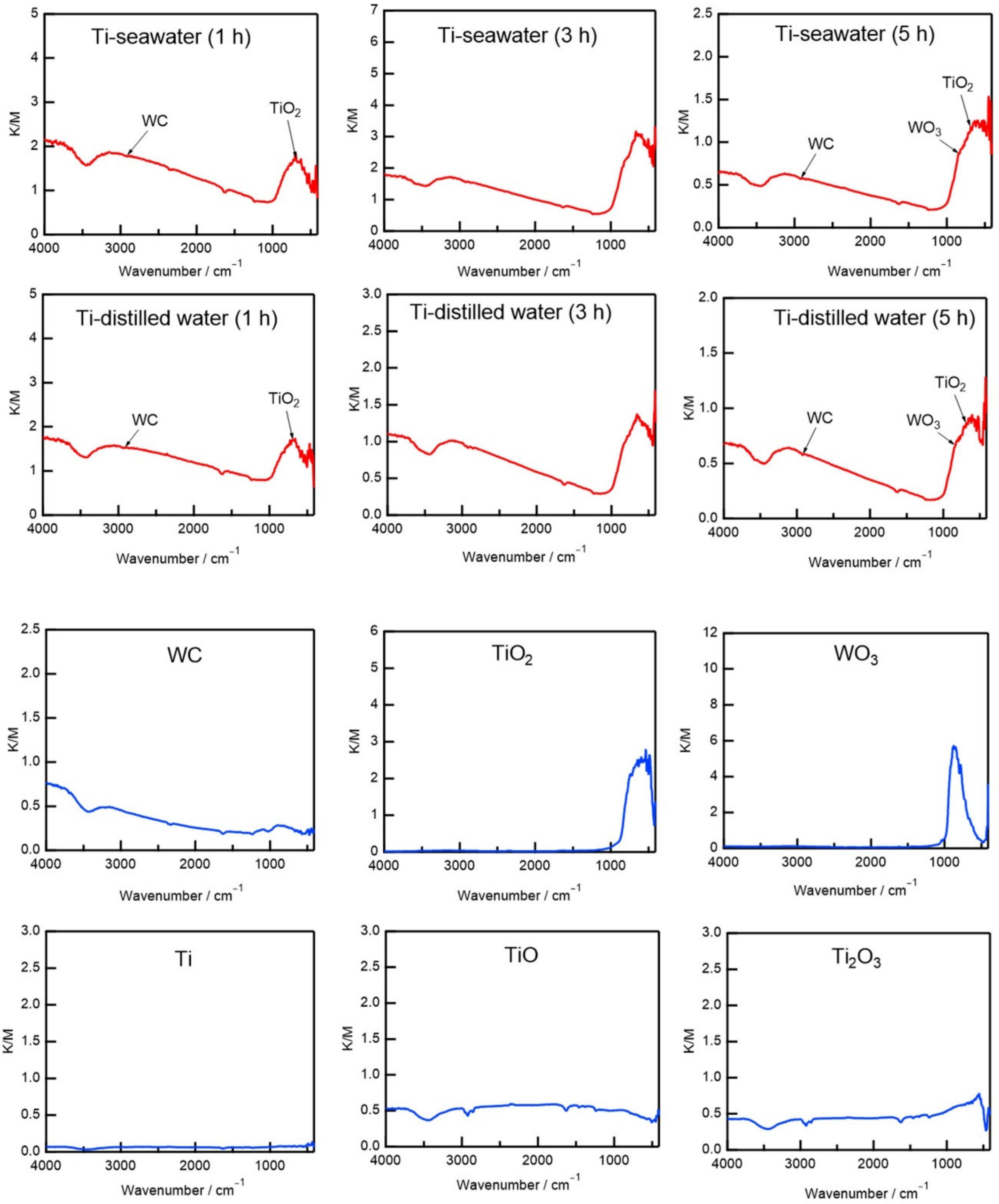

Fig. S10. FTIR spectra of solid products and standard samples. FTIR spectra of mechanochemical Ti–seawater and Ti–distilled water reaction products (red lines). The samples were prepared from the solid products of 1-, 3-, and 5-h reactions. For clarity, several standard samples were purchased and used as received for similar measurements (blue lines). K/M is the Kubelka–Munk absorption coefficient, i.e., the absorbance as measured by the diffuse reflectance method.

Note S9. Raman and XPS spectra of WO_3

Fig. S11 shows the Raman spectra of the products of the mechanochemical Ti–water (red line) and WC–water (black line) reactions carried out using the WC milling medium; a milling time of 10 h was used in each case. Four WO_3 Raman bands can be identified: the W–O–W bending mode [i.e., δ(W–O–W)] at 270 cm^{-1}, W–O–W stretching modes at 700 and 810 cm^{-1} [i.e., ν(W–O–W)], and the W=O stretching mode at 960 cm^{-1} [i.e., ν(W=O)]. These Raman bands were assigned based on literature results.[22,23] The TiO_2 Raman bands are located at 400, 520, and 640 cm^{-1}, and these contributed a broad increase in intensity to the spectrum of the products of the mechanochemical Ti–water reaction (red line in Fig. S11). The spectra were acquired using a Horiba Jobin Yvon HR800 Raman spectrometer and an excitation wavelength of 632.8 nm.

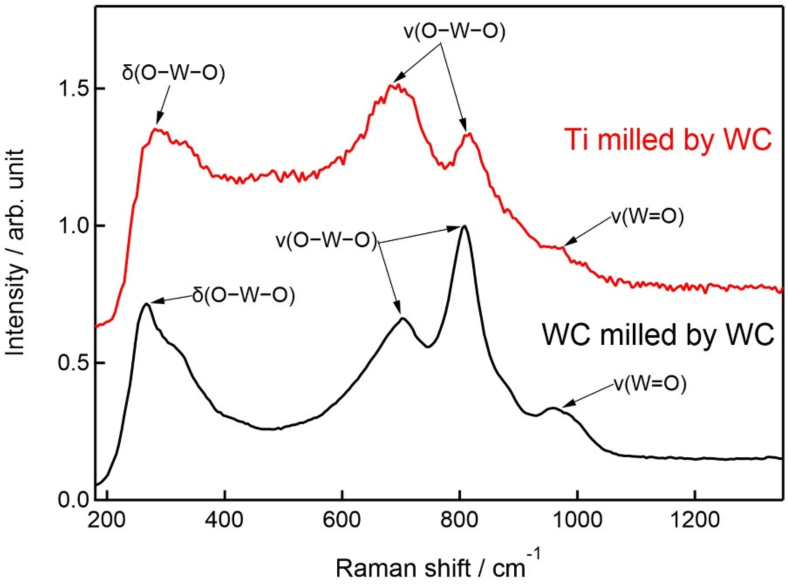

Fig. S11. Raman spectra of products of the mechanochemical Ti–water reaction performed using the WC milling medium. The reaction was conducted at a revolution velocity of 400 rpm. Assignments for the WO_3 Raman bands observed in the spectrum are overlaid on the plot.

Fig. S12 shows the X-ray photoelectron spectroscopy (XPS) spectra of the products (samples 1−4) of the mechanochemical Ti–water (Fig. S12a,b) and TiO_2–water (Fig.S12 c,d) reactions carried out using the WC milling medium; a reaction time of 8 h or 3h was used in each case. Each spectrum (W 4d) shows WO_3 bands, and longer reaction times gave higher relative ratio of WO_3 bands. The spectra were acquired using a spectrometer (Kratos Ultra2, Shimadzu) and an excitation X-ray of monochromatic AlKα.

Sample	1	2	3	4
Reaction	Ti−H_2O	Ti−H_2O	TiO_2−H_2O	TiO_2−H_2O
Reaction time (h)	8	3	8	3

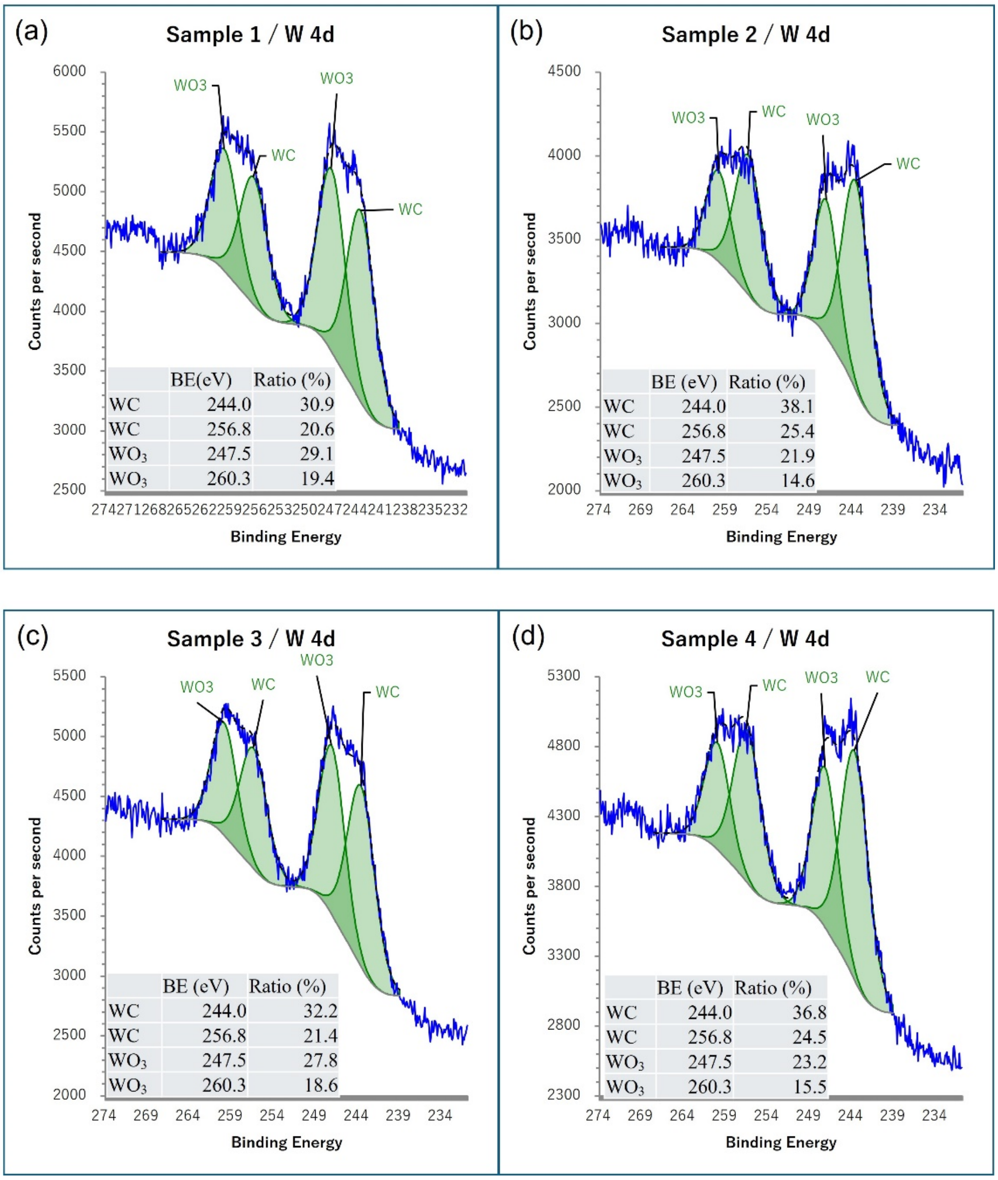

(a)

	BE(eV)	Ratio (%)
WC	244.0	30.9
WC	256.8	20.6
WO_3	247.5	29.1
WO_3	260.3	19.4

(b)

	BE (eV)	Ratio (%)
WC	244.0	38.1
WC	256.8	25.4
WO_3	247.5	21.9
WO_3	260.3	14.6

(c)

	BE (eV)	Ratio (%)
WC	244.0	32.2
WC	256.8	21.4
WO_3	247.5	27.8
WO_3	260.3	18.6

(d)

	BE (eV)	Ratio (%)
WC	244.0	36.8
WC	256.8	24.5
WO_3	247.5	23.2
WO_3	260.3	15.5

Fig. S12. XPS spectra (W 4d) of products of the mechanochemical (a, b) Ti–water and (c, d) TiO_2−water reactions performed using the WC milling medium. The reactions were conducted at a revolution velocity of 400 rpm. WO_3 bands are observed in all spectra, and their binding energy (BE) and relative ratio are listed in tables as inset.

Note S10. H_2 produced by milling Ti and WC powders together with water using ZrO_2 milling medium

We investigated the mechanochemical generation of H_2 from a mixture of Ti and WC powders milled with a ZrO_2 milling medium (vessel and balls). Extraordinary H_2 generation was observed, and the maximum yield was 150%, as shown in Fig. S13. This yield was smaller than that observed when WC was used as the milling medium (300%), as shown in Fig. 1F. The reason for this lower yield was attributed to the following two factors. First, when ZrO_2 rather than WC was used, the collision energy was lower, as the former has a lower density and Young's modulus (Table S7), even though the revolution velocity used for milling with ZrO_2 (500 rpm, Fig. S12) was higher than that used for milling with WC (400 rpm, Fig. 1F). Specifically, for the WC milling medium, the cumulative collision energy as calculated using Eqn (S25)–(S28) was 120% higher, which resulted in higher reaction efficiency and hence also a higher yield. Second, the reaction system consisting of the ZrO_2 milling medium and two powders was inefficient. This was because extraordinary H_2 production via the mechanochemical TiO_2–water reaction occurred owing to the fact that individual TiO_2 and WC particles were in contact while being crushed within a region of high-T, high-p water between a pair of ZrO_2 balls. In contrast, using the WC milling medium, extraordinary H_2 production occurred simply owing to the fact that individual generated TiO_2 particles were crushed in high-T, high-p water between pairs of WC balls. Therefore, the reaction efficiency was much higher for the use of the WC milling medium.

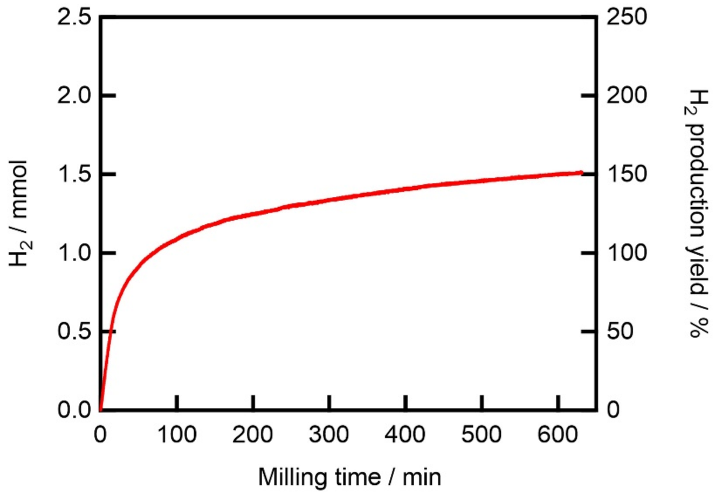

Fig. S13. H_2 production during the mechanochemical reactions between Ti powder, WC powder, and water. The milling medium was ZrO_2 and the revolution velocity was 500 rpm.

Note S11. XRD of products of mechanochemical Ti–water and TiO_2–water reactions

Mechanochemical reactions using WC milling medium

We performed XRD measurements on the solid products of the mechanochemical Ti–water and TiO_2 (anatase)–water reactions performed using the WC milling medium, and the diffraction patterns are shown in Fig. S14a and b, respectively. The patterns in Fig. S14a and b feature strong WC signals generated by the milling medium. TiO signals can also be seen in the patterns in Fig. S14a and b, generated by the mechanochemical Ti–water (oxidation of Ti to generate H_2) and TiO_2–WC (reduction of TiO_2 by WC) reactions, respectively. We did not identify WO_3 signals in the XRD patterns because XRD characterizes the bulk structure of crystalline materials, and the conversion of WC to WO_3 proceeded on the WC surfaces. The Raman spectrum, which includes signals generated at depths below the WC surface of up to 100 nm, included a WO_3 band (Fig. S11), and the FTIR spectrum of the products of the catalytic mechanochemical Ti/TiO_x–water reactions also included WO_3 bands (Fig. S10). In addition, XPS spectra also showed WO_3 bands (Fig. S12). Thus, mechanochemical Ti–water and TiO_2–water reactions performed using the WC milling medium produced TiO and WO_3. Next, because the WC milling medium contained 12% Co as a binder, we looked for signals assignable to $CoWO_4$, another possible product of the mechanochemical reactions performed using the WC milling medium, in the XRD pattern (Fig. 14). However, we did not observe any such signals.

The experimental methods and sample preparation procedures used to obtain the XRD patterns were similar to those described in Note S4. Briefly, the reactions were conducted using 4 mmol of Ti or TiO_2 (anatase), 10 mL of distilled water, and the WC milling medium. In each case, the revolution velocity was 400 rpm and the reaction time was 100 min. After the mechanochemical reactions, the slurries in the vessel were collected by centrifugation at 7830 rpm for 20 min (Centrifuge 5430, Eppendorf), and the obtained precipitates were dried at 35 °C overnight before the XRD measurements were acquired with Cu Kα radiation (40 kV, 30 mA; Smart lab, Rigaku, Japan). A sample-holder plate made from nonreflecting silicon, custom-designed to guarantee a background-free signal, was used to acquire the measurements.

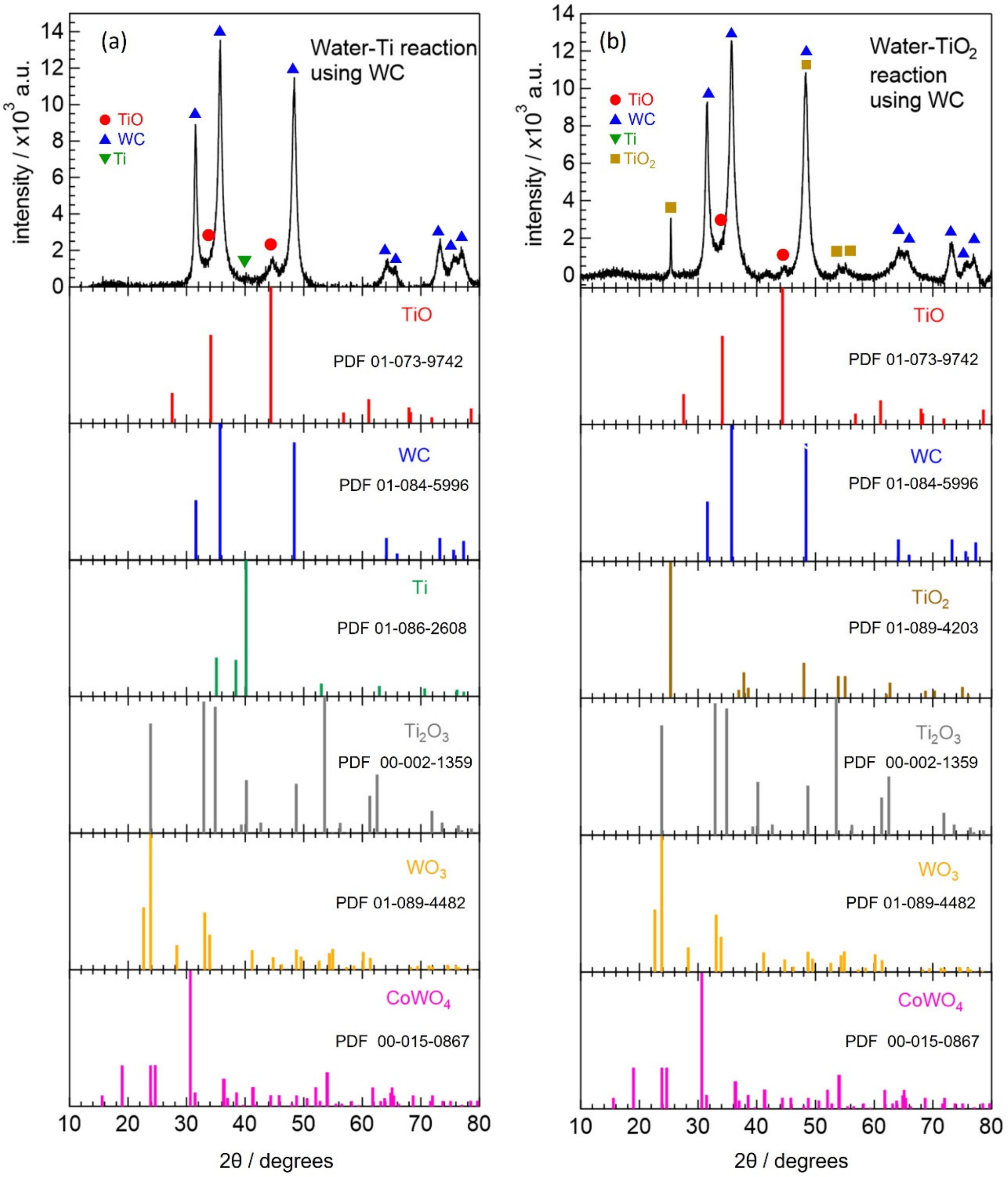

Fig. S14. XRD patterns of products of the mechanochemical (a) Ti–water and (b) TiO_2–water reactions performed using the WC milling medium. The bar XRD patterns of the standard materials were generated using powder diffraction data from the International Centre for Diffraction Data (ICDD) database. The data shown for TiO_2 and WO_3 are patterns for anatase and the α phase, respectively. The numbers embedded in each data indicate the ICCD PDF of their crystal structures.

Mechanochemical reactions using SUS milling medium

We performed XRD measurements on the solid products of the mechanochemical Ti–water and TiO_2 (anatase)–water reactions performed using the SUS milling media, and the resulting diffraction patterns are shown in Fig. S15a and b, respectively. The patterns in Fig. S15a and b include Fe_3O_4 signals originating from the milling medium. Ti_2O_3 (and TiO) signals can also be observed in the patterns in Fig. S15a and b. These materials were generated by the mechanochemical Ti–water (oxidation of Ti to generate H_2) and/or TiO_2–Fe (reduction of TiO_2 by Fe in SUS) reactions. Therefore, the Fe present in SUS acted as a mechano-cocatalyst, facilitating the production of extraordinary amounts of H_2 via mechanochemical Ti/TiO_2–water reactions performed using the SUS milling medium (Fig. 2A and B). This conclusion is further supported by the fact that signals that could also be assigned to the cocatalytic byproduct (Fe_3O_4) were observed in the XRD patterns (Fig. S15). The experimental methods and sample preparation procedures used to obtain the patterns shown in Fig. 15 were the same as those described on page S24, except that the SUS milling medium was used in place of the WC milling medium.

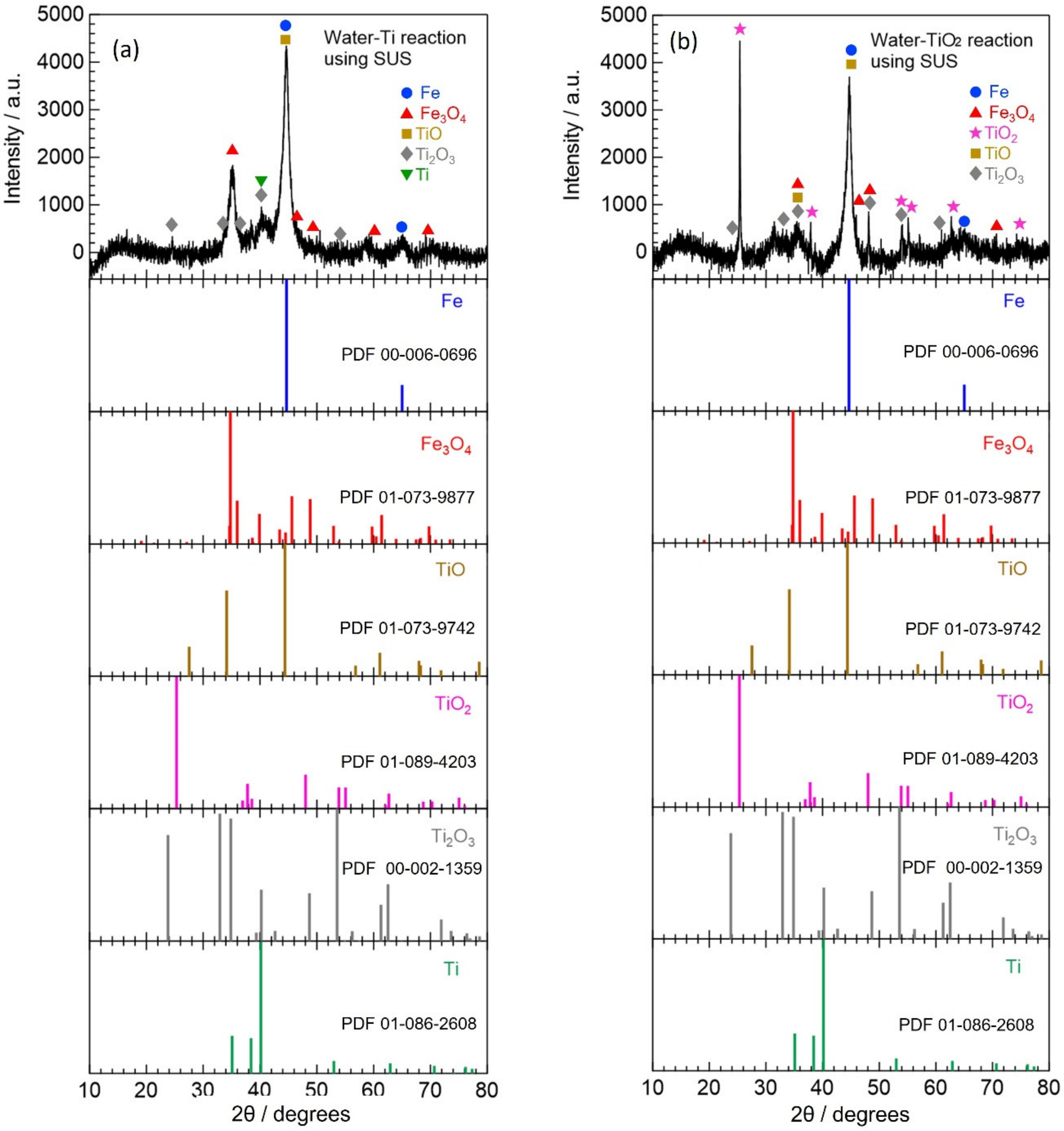

Fig. S15. XRD patterns of products of the mechanochemical (a) Ti–water and (b) TiO_2–water reactions performed using the SUS milling medium. The bar XRD patterns of the standard materials were generated using powder diffraction data from the International Centre for Diffraction Data (ICDD) database. The data shown for TiO_2 and WO_3 are patterns for anatase and the α phase, respectively. The numbers embedded in each data indicate the ICCD PDF of their crystal structures.

Note S12. Theoretical local *p* and *T* calculations

Local pressure at the point of impact between balls

The impulsive pressure was calculated using Hertz theory,[24,25] as summarized below:

$$\langle\sigma^*\rangle = 1.3\rho^{0.2}\theta_1^{-0.8}W^{0.4} \tag{S18}$$

$$\theta_1 = \frac{4(1-\nu_1^2)}{e_1} \tag{S19}$$

$$W = \omega_1 l_2|(\kappa+1)^2 + \Gamma^2 - 2\Gamma(\kappa-1)\cos\varphi + (\Gamma+1)^2|^{0.5} \tag{S20}$$

In Eqn (S18)–(S20), $\langle\sigma^*\rangle$ is the instantaneous pressure of the sample between two balls, ρ is the density of each individual milling ball, θ_1 is the compliance constant of the sample, W is the relative velocity of the milling balls, ν_1 is Poisson's ratio for the sample, e_1 is Young's modulus for the sample, ω_1 is the angular frequency associated with the revolution of the vessel, l_2 is the inner radius of the vessel, κ is the velocity ratio (rotations/revolutions), Γ is the distance ratio l_1/l_2 (l_1 is the distance between the rotation and revolution axes), and φ is the angle of the ball leaving the vessel wall. Although the instantaneous and atmospheric pressures were summed to determine the local pressure, the local pressure was almost equal to the impulsive pressure because the atmospheric pressure was, relatively, negligible. The ball-to-ball contact region radius r (~50 μm) during impact was calculated using the equation $r = 0.75R_0\rho^{0.2}\theta_1^{0.2}W^{0.4}$, where R_0 = 0.8 mm is the radius of the ball. The ball-to-ball contact period τ during impact was calculated to be ~10^{-6} s using the equation $\tau = 3.6R_0\rho^{0.4}\theta_1^{0.4}W^{-0.2}$, and the parameters used to obtain this value are listed in Tables S6 and S7.

Local temperature at the point of impact between balls

The local *T* between colliding balls was calculated using Hertz theory.[24,25] Briefly, the impulsive *p* increases the local *T*, and the magnitude of the change depends on the thermal properties and tribology of the sample over a frictional interaction time. The local *T* was obtained by summing the measured bulk *T* and impulsive Δ*T*, which was calculated as follows:

$$\Delta T(x,t) = 2Q(c_1^2\lambda_1^2\rho_1^2)^{-0.25}\{t^{0.5}\mathrm{iErfc}\left[\frac{x}{2}(a_1^2)^{0.25}t^{0.5}\right]$$

$$-(t-\tau_1)^{0.5}\mathrm{iErfc}\left[\frac{x}{2}(a_1^2)^{0.25}(t-\tau_1)^{0.5}\right]\} \tag{S21}$$

$$\tau_1 = 4.0R_1\rho_1^{0.5}\rho^{-0.1}\theta_1^{0.4}W^{-0.2} \tag{S22}$$

$$2Q = \xi\langle\sigma^*\rangle W_t^* \tag{S23}$$

$$W_t^* = 0.38\rho_1^{-0.5}\rho^{0.3}\theta_1^{-0.2}W^{0.6} \tag{S24}$$

where c_1 is the heat capacity, λ_1 is the thermal conductivity, ρ_1 is the density of the sample, t is time, iErfc is the integral error expressed as iErfc[0] = 0.5642, τ_1 is the friction interaction time for the collisions between two sample particles (~10^{-9} s), $\langle\sigma^*\rangle$ is the impulsive pressure, W_t^* is the relative velocity associated with particle interaction, ρ is the density of the ball material, θ_1 is the compliance coefficient of the sample, W is the relative velocity of the balls, and ξ is the dynamic friction coefficient. The radius of the contact region r_1 (~50 nm) between particles during impact was calculated using the equation $r_1 = 0.75R_1\rho^{0.2}\theta_1^{0.2}W^{0.4}$, where R_1 is the radius of a particle. The parameters used in these calculations are listed in Tables S6, S7, and S9.

Milling ball collision energy

The collision energy was obtained from the kinetic energy of a single milling ball:

$$E = \frac{1}{2}mv^2 \tag{S25}$$

where m is the weight and v is the velocity of a single ball ($v = W/2\pi$).

The total collision energy in the milling vessel was summed over the number of balls:

$$E_\mathrm{t} = \frac{1}{2}mv^2N\frac{1}{M} \tag{S26}$$

where E_t is the total collision energy in the vessel, N is the number of milling balls, and M is the molar amount of the sample. The cumulative collision energy E_tc was obtained using Eqn (S26):

$$E_\mathrm{tc} = E_\mathrm{t}z \tag{S27}$$

$$z = \sqrt{2}vsn \tag{S28}$$

where z is the collision frequency, s is the collision cross section ($s = \pi d^2$, where d is the ball diameter), and n is the number density of the balls in the vessel. The parameters used for this calculation for each milling medium are listed in Table S7.

Note S13. H_2 production rates normalized by the consumed electric power

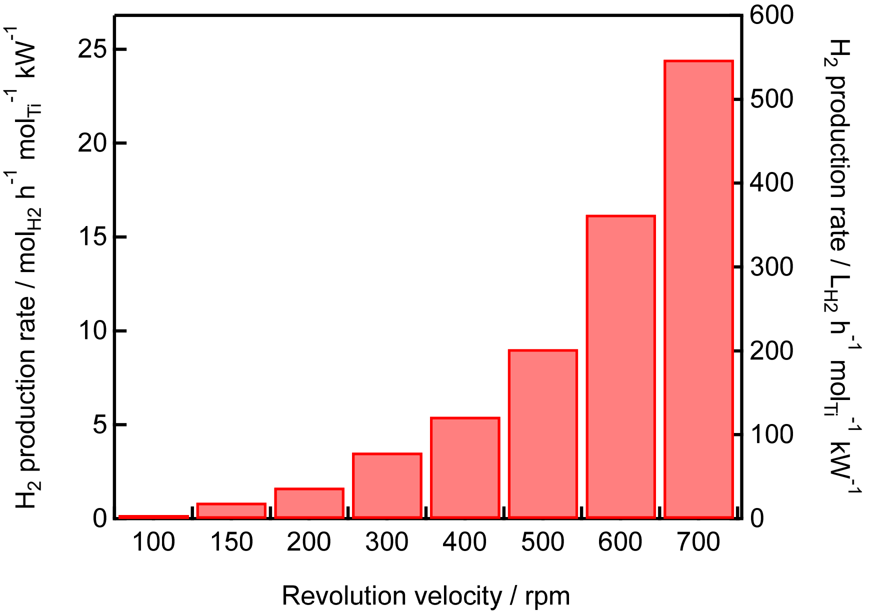

Fig. S16. H_2-production rates. These data were obtained by normalizing the data in Fig. 4F by the consumed electric power. The left and right axes show H_2-production rates in molar ($mol_{H2}\ h^{-1}\ mol_{Ti}^{-1}\ kW^{-1}$) and standard-state volume ($L_{H2}\ h^{-1}\ mol_{Ti}^{-1}\ kW^{-1}$) units, respectively.

Note S14. SEM images, ICP-OES, and GC data

SEM images of metal powders

To evaluate the morphologies before and after milling of the metal particles used in the mechanochemical metal–water reactions, we performed scanning electron microscopy (SEM; S-3400N, Hitachi High-Tech). Fig. S17 and S18 show SEM images of samples of the six metal powders before and after milling, respectively; the insets show the corresponding size distributions obtained by analyzing the SEM images using ImageJ software.

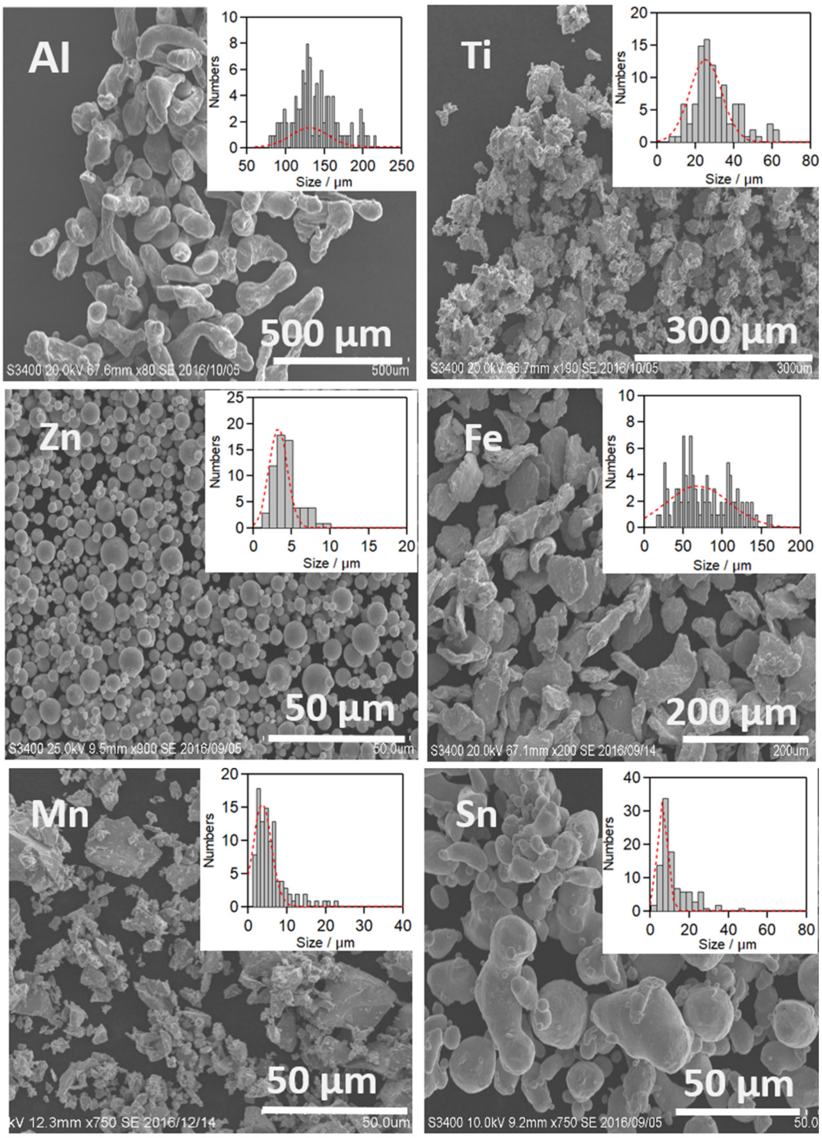

Fig. S17. SEM images of various metal powders before milling.

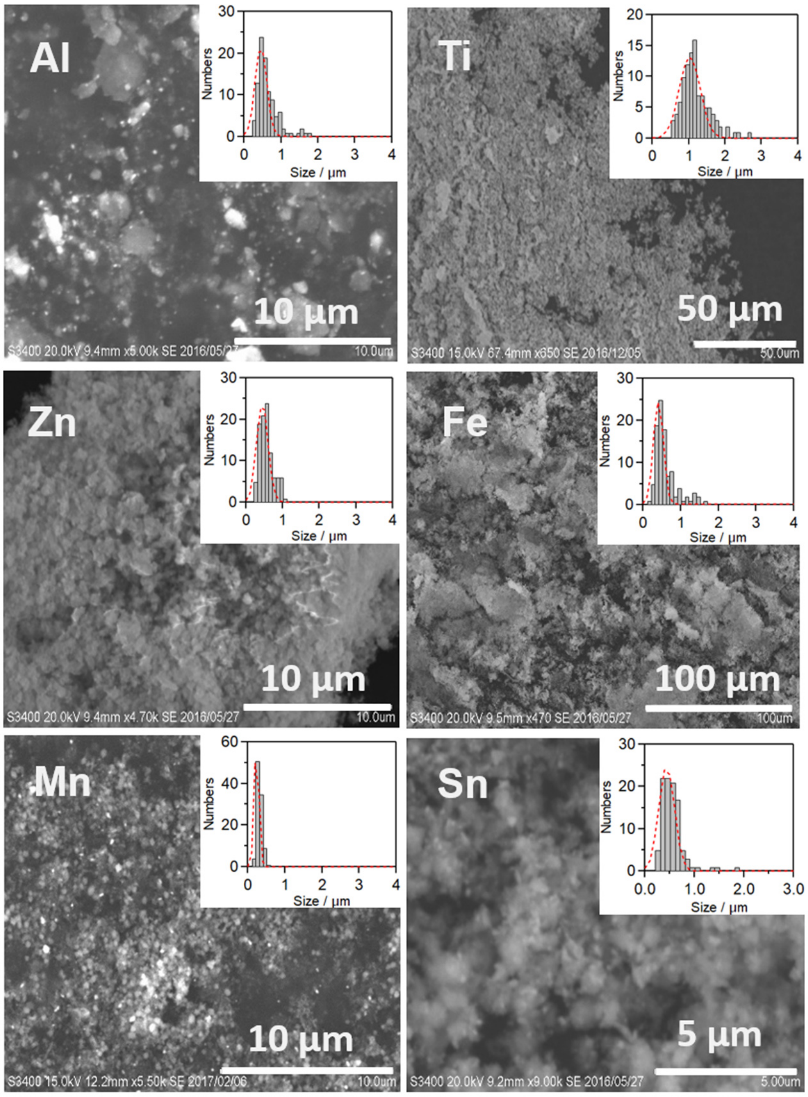

Fig. S18. SEM images of various metal powders after milling. Milling was conducted in distilled water for 10 h at a revolution velocity of 400 rpm.

SEM images and mechanochemical reactions of titanium oxides

The particle sizes of the three titanium oxides (TiO, Ti_2O_3, and TiO_2) were measured using SEM. Fig. S19 shows the SEM images and size distributions of particles from samples of the three types of titanium oxide before milling; the average radii are listed in Table S10. There were large differences between the particle sizes of the different oxides; specifically, the TiO_2 particles were more than 20 times smaller than the TiO and Ti_2O_3 particles. In contrast, in terms of the mechanical properties and hardness, the differences between the different types of titanium oxide are relatively small (Table S10). Therefore, because the H_2 production via mechanochemical reactions between water and the three titanium oxides proceeded similarly, we conclude that under the conditions of this experiment, the particle sizes of the titanium oxides seem to have had a negligible effect on mechanochemical H_2 production by milling in water (Fig. 3). In fact, our previous study showed that during the initial milling period, within 10–20 min, the particle size was reduced from a few tens of micrometers to a few hundred nanometers,[26] and in the current experiments, the reaction (milling) time was long (up to 10 h). Since the all the titanium oxide particles were reduced to similar sizes during the initial period of milling, it can be concluded that the reactions of the different titanium oxides were independent of the initial particle size.

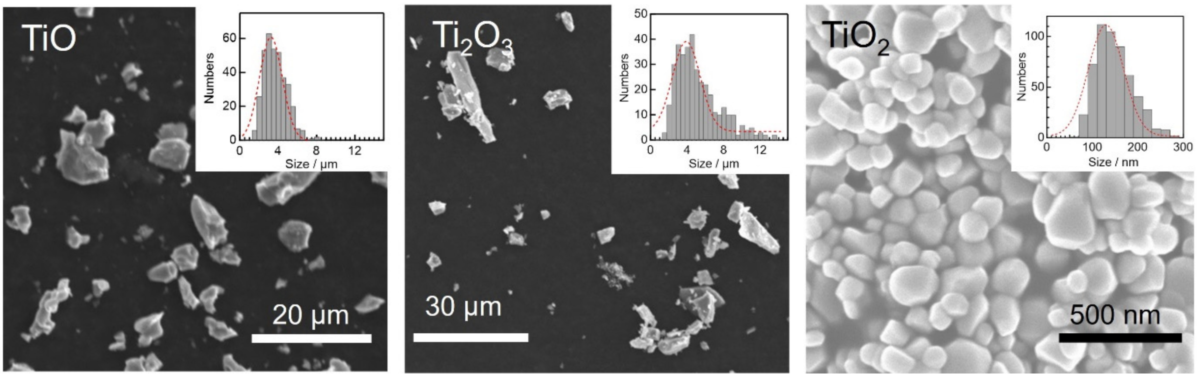

Fig. S19. SEM images of TiO, Ti_2O_3, and TiO_2 powders.

SEM images of milling balls before and after mechanochemical reactions

To examine the surface morphology of the milling balls, we performed SEM (Fig. 20). From the resulting images, we concluded that the differences between the morphology of the balls before and after the mechanochemical reactions were insignificant.

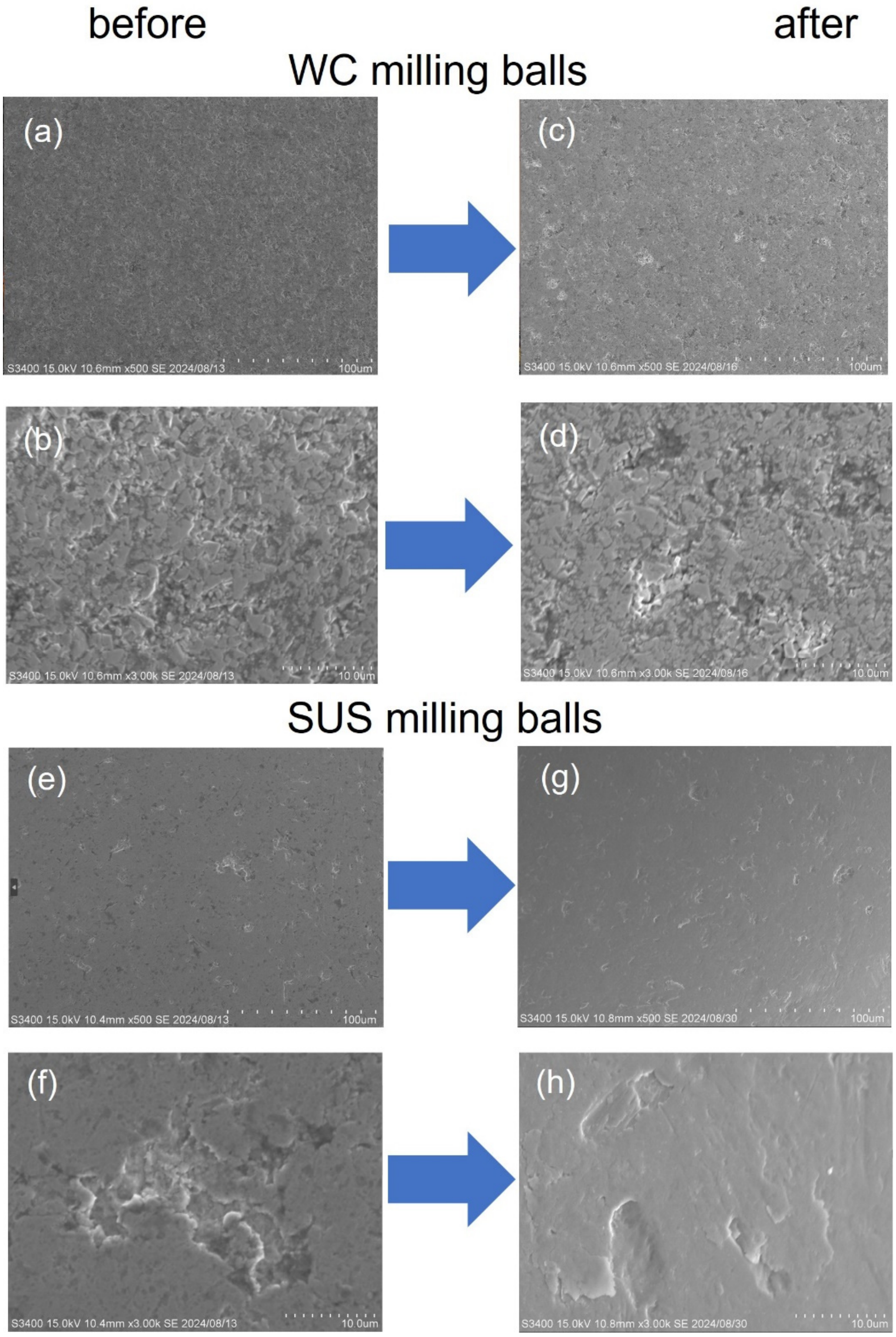

Fig. S20. SEM images of milling balls before (left) and after (right) mechanochemical Ti–water reactions using (a–d) WC and (e–h) SUS milling media. Reactions were conducted at a revolution velocity of 400 rpm for a period of 5 h.

ICP-OES measurements of aqueous solution after mechanochemical reactions

We quantified the W and Fe content of the aqueous solutions in the milling vessel after the mechanochemical Ti–water reactions performed using the WC and SUS milling media, respectively. We measured the concentrations of these elements in the supernatant from the vessel using inductively coupled plasma–atomic emission spectroscopy (ICP-OES; 700 series, Agilent technologies). The aqueous solution samples were prepared by mechanochemically reacting Ti and distilled water (400 rpm, reaction time 5 h). The obtained slurry was centrifuged at 7830 rpm for 20 min (Centrifuge5430, Eppendorf). The supernatant was obtained by filtering using a PTFE cartridge filter with a pore size of 0.45 μm and used for ICP-OES measurements performed under aqueous flow conditions. By analyzing the ICP-OES data, we established that the concentrations of these elements in the aqueous reaction solution were <1 ppm (Fig. S21).

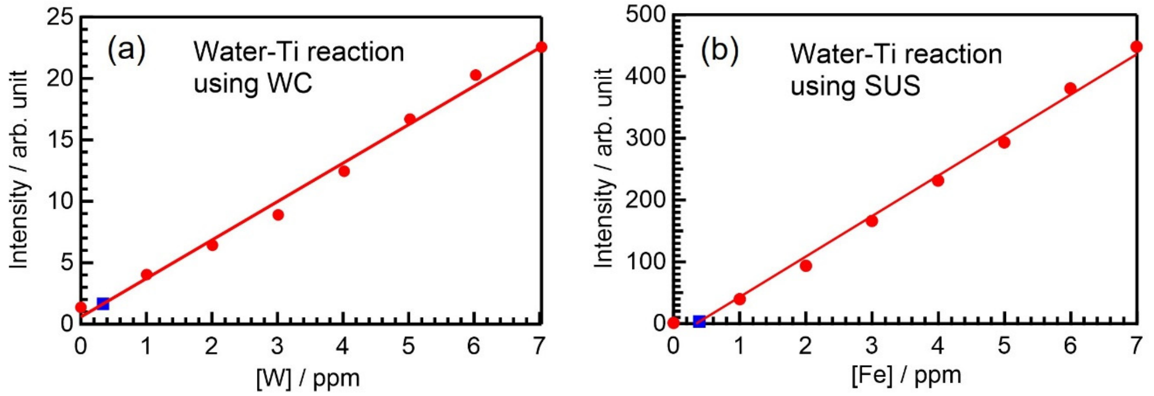

Fig. S21. ICP-OES analyses of elements in the aqueous solutions after the mechanochemical Ti–water reactions performed using the (a) WC and (b) SUS milling media. The red solid circles show the data for standard solutions used to construct the calibration curve. The blue squares show the results for the sample solutions.

Qualitative and quantitative GC measurement data

Table S1. GC retention times for standard gases in He carrier gas

Standard gas	Retention time (min)
H_2	0.8
O_2	2.2
N_2	2.4
CH_4	7.8
CO_2	24.5
CO	3.2

Table S2. GC signal intensity (sensitivity) as measured using 100 μL of the sample gas with He or Ar as the carrier gas

Standard gas	Intensity (10^4 μV)	
	He	Ar
H_2	1.9	124
O_2	92.2	14
N_2	94.1	10.8
CH_4	30.2	16.7
CO_2	12.7	10.6

Note S15. H_2 amounts, thermodynamics, and material properties

H_2 amounts produced by the mechanochemical metal–water reactions and standard Gibbs energy analyses

Table S3 lists the H_2 amounts produced by the metal–water reactions in the present study. The data were obtained from Fig. 1E (milling time: 600 min). To analyze the dependence of the reaction efficiency on the reactant metal, we evaluated the standard Gibbs energies of typical corrosion reactions. The standard electrode potentials and standard Gibbs energies listed in Table S3 do not relate specifically to the mechanochemical reactions but are typical data used to generate electrochemical series and for thermodynamic calculations.[27–29] The standard Gibbs energies are plotted on the horizontal axis of Fig. 2D.

Table S3. Amounts of H_2 produced by mechanochemical metal–water reactions and standard Gibbs energies of oxidation

Metals	Amount of H_2 produced (mmol)[a)]	Amount of H_2 produced per mole of metal ($\mathrm{mol_{H2}\ mol_{metal}^{-1}}$)[b)]	Standard potential $E°$ (V)[c)]	Oxidation number n	$\Delta G°$ ($\mathrm{kJ\ mol^{-1}}$)[d)]
Al	3.1	1.5	1.66	3	−481
Ti	13.8	6.9	1.63	2	−314
Zn	1.8	0.9	0.76	2	−147
Fe	2.4	1.2	0.44	2	−84.9
Mn	2.0	1.0	1.18	2	−228
Sn	0.3	0.15	0.14	2	−27
W	2.1	1.1	0.09	6	−52.1

[a)] Data obtained from the H_2 amount after 600 min of milling, as shown in Fig. 1E (all of the data except the W–water data) or Fig. S5 (the W–water data); [b)] data obtained by dividing the amount by 2 mmol, which was the amount of metal used as the reagent for each experiment; [c)] standard potentials for oxidation half-reaction, i.e., standard oxidation potentials; [d)] $\Delta G°$ was obtained from the equation $\Delta G^{\circ} = -nFE^{\circ}$, where F is the Faraday constant, E° is the standard potential for oxidation of the metal to a state with oxidation number n. For the case of the oxidation half reaction, E° is equal to the cell potential with respect to the standard hydrogen electrode). The values of E° were obtained from ref. 27 (all of the data except the W–water data) or ref. 29 (the W–water data).

Standard Gibbs energies and activation energies of H_2-producing metal–water reactions

To better understand the amount of H_2 produced by the metal–water reactions, we obtained the standard Gibbs energies $\Delta G_r°$ by considering the thermodynamics of the reactions, using a method detailed in a physical chemistry textbook[27]; the procedure used is outlined as follows for the example of the reaction between Ti and water:

$$Ti + 2\ H_2O \rightarrow TiO_2 + 2\ H_2 \tag{S29}$$

$$\Delta G_r° = \Delta G°(\text{products}) - \Delta G°(\text{reactants}) \tag{S30}$$

It should be emphasized that the obtained values listed in Table S4 are not the thermodynamic parameters of the experimental mechanochemical reactions but were instead obtained by considering the thermodynamics of the reactions.

Table S4. Standard Gibbs energies and activation energies for H_2-producing metal–water reactions

Metals	Chemical equations	$\Delta_r G°$ (kJ mol^{-1})[a)]	E_a (kJ mol^{-1})[b)]	refs.
Al	$Al + 3\ H_2O \rightarrow Al(OH)_3 + 3/2\ H_2$	−594.3	50	30,31
Ti	$Ti + 2\ H_2O \rightarrow TiO_2 + 2\ H_2$	−410.1	36	30
Zn	$Zn + H_2O \rightarrow ZnO + H_2$	−81.1	35	30
Fe	$Fe + 4/3\ H_2O \rightarrow 1/3\ Fe_3O_4 + 4/3\ H_2$	−22.3	8	30
Mn	$Mn + 4/3\ H_2O \rightarrow 1/3\ Mn_3O_4 + 4/3\ H_2$	−111.5	22	30
Sn	$Sn + H_2O \rightarrow SnO + H_2$	−14.6	31	30,32

[a)]Values obtained for the use of 1 mol of the metal; [b)]values obtained from ref. 14.

Standard Gibbs energies of metal oxide reduction reactions

To investigate the reduction reactions of the metal oxides, we obtained the standard Gibbs energies $\Delta G_r°$ based on thermodynamic data, via the method detailed in a physical chemistry textbook[27] similar to that outlined in the preceding section of this note (*Standard Gibbs energies and activation energies of H_2-producing metal–water reactions*). Note that the obtained values listed in Table S5 are not experimental mechanochemical reaction data but were obtained based on thermodynamic considerations.

The ΔG values for the reduction of ZnO and/or SnO with O_2 generation are smaller than that for the reduction of TiO_2 with O_2 generation (Table S5). However, these three reactions are not relevant to the present systems because O_2 gas generation was not detected for any of the reactions investigated in this study. In addition, we concluded that the continuous H_2 processes occurred via a catalytic cycle not because of the value of ΔG for the reduction reaction but after considering the overall energy of the reaction, which is dependent on the following three magnitudes: i) ΔG for the oxidation of the metal via metal–water reactions to generate H_2, ii) ΔG for the reduction of metal oxides via the reaction between the metal oxides and milling medium (WC or SUS), and iii) the activation energies of both of the above-mentioned reactions. Moreover, an element with multiple valence states having similar energies, such as Ti (Fig. 2E), was required for efficient catalyst regeneration over the course of multiple redox cycles; however, Zn and Sn do not possess such states. Thus, we concluded that the Ti/TiO_2 system exhibited selective, continuous catalytic H_2 production owing to the overall energy balance of the reaction and the electronic structure of Ti.

Table S5. Standard Gibbs energies for metal oxide reduction reactions

Metal oxide	Chemical equation	$\Delta_r G°$ (kJ mol^{-1})
$Al(OH)_3$	$Al(OH)_3 \rightarrow Al + 3/2\ H_2 + 3/2\ O_2$	1305.8
TiO_2	$TiO_2 \rightarrow Ti + O_2$	884.5
ZnO	$ZnO \rightarrow Zn + 1/2\ O_2$	318.3
Fe_3O_4	$Fe_3O_4 \rightarrow 3\ Fe + 2\ O_2$	1015.5
MnO_2	$Mn_3O_4 \rightarrow 3\ Mn + 2\ O_2$	1283.3
SnO	$SnO \rightarrow Sn + 1/2\ O_2$	251.8

Mechanical properties used to calculate conditions between colliding balls

Table S6. Ti and TiO_2 parameters used in calculations

Parameters	Ti	TiO_2
Density ρ_1 (g cm^{-3})	4.51[a)]	3.84[a)]
Poisson's ratio ν_1	0.361[b)]	0.280[a)]
Young's modulus e_1 ($\times10^{10}$ dyn cm^{-2})	120.2[b)]	283.0[a)]
Compliance coefficient θ_1 ($\times10^{-12}$ cm^2 dyn^{-1})	2.89[b)]	1.30[a)]
Thermal conductivity λ_1 ($\times10^5$ erg cm^{-1} K^{-1} s^{-1})	21.6[b)]	8.37[c)]
Specific heat capacity c_1 ($\times10^6$ erg g^{-1} K^{-1})	5.28[b)]	6.90[d)]
Particle radius R_1 ($\times10^{-5}$ cm)	6.0[e)]	6.0[e)]
Dynamic friction coefficient ξ	0.47[f)]	0.37[g)]

[a)]Ref. 33; [b)]ref. 34; [c)]ref. 35; [d)]ref. 36; [e)]average radius of Ti in Fig. S13 and S14; [f)]ref. 37; [g)]ref. 38.

Table S7. Milling media parameters

Parameters	WC	SUS	ZrO_2
Young's modulus e ($\times10^{10}$ dyn cm^{-2})	509	198	210
Density ρ (g cm^{-3})	14.3	7.80	6.00
Poisson's ratio	0.21	0.275	0.30
Weight of a single ball m (g)	0.0307	0.0167	0.0129
Number of milling balls N	3261	3168	3015
Collision cross section s (cm^2)	0.080	0.080	0.080
Number density of ball n (cm^{-3})	42.7	41.5	39.5

Standard Gibbs energy of the reaction between TiO_2 and the mechano-cocatalyst

To better understand the H_2 produced by the reaction between TiO_2 and the milling medium (WC or SUS), we evaluated the standard enthalpy ($\Delta H°$), entropy ($\Delta S°$), and Gibbs energy ($\Delta G°$) from thermodynamic data using the procedure described as follows, based on a method outlined in a physical chemistry textbook,[7] for the example of the reaction between TiO_2 and WC:

$$TiO_2 + 2/3\ WC \rightarrow Ti + 2/3\ WO_3 + 2/3\ C \tag{S31}$$

$$\Delta_r H° = \Delta H°(\text{products}) - \Delta H°(\text{reactants}) \tag{S32}$$

Note that the obtained values listed in Table S8 are not mechanochemical reaction data, but typical data calculated from thermodynamic quantities.[30,39,40]

Table S8. Chemical equations and standard Gibbs energies for TiO_2 reduction by various mechano-cocatalysts

Mechano-cocatalyst	Products	Chemical equations	$\Delta_r H°$ (kJ mol^{-1})[b]	$\Delta_r S°$ (J mol^{-1} K)[b]	$\Delta_r G°$ (kJ mol^{-1})[b]	$\Delta_r G$ (kJ mol^{-1})[b]		refs.
						700 K	1500 K	
WC	Ti	$TiO_2 + 2/3\ WC$ $\rightarrow Ti + 2/3\ WO_3 + 2/3\ C$	404.8	13.6	400.9	395.3	384.5	30, 39
WC	TiO	$TiO_2 + 1/3\ WC$ $\rightarrow TiO + 1/3\ WO_3 + 1/3\ C$	129.6	1.3	129.4	128.7	127.7	30, 39, 40
WC	Ti_2O_3	$TiO_2 + 1/6\ WC$ $\rightarrow 1/6\ Ti_2O_3 + 1/6\ WO_3 + 1/6\ C$	45.5	−2.3	46.5	47.2	49.0	30, 39
Fe[a]	Ti	$TiO_2 + 3/2\ Fe$ $\rightarrow 1/2\ Fe_3O_4 + Ti$	380.5	13.0	376.8	371.4	361.0	30
Fe[a]	TiO	$TiO_2 + 3/4\ Fe$ $\rightarrow 1/4\ Fe_3O_4 + TiO$	117.4	1.0	117.3	116.7	116.0	30, 40
Fe[a]	Ti_2O_3	$TiO_2 + 3/8\ Fe$ $\rightarrow 1/8\ Fe_3O_4 + 1/2\ Ti_2O_3$	39.5	−2.5	40.5	41.2	43.1	30
Cr[a]	Ti	$TiO_2 + 4/3\ Cr$ $\rightarrow 1/3\ Cr_2O_3 + Ti$	179.9	3.2	179.1	177.7	175.2	30
Cr[a]	TiO	$TiO_2 + 2/3\ Cr$ $\rightarrow 1/3\ Cr_2O_3 + TiO$	17.1	−3.9	18.5	19.9	23.0	30, 40
Cr[a]	Ti_2O_3	$TiO_2 + 1/3\ Cr$ $\rightarrow 1/6\ Cr_2O_3 + 1/2\ Ti_2O_3$	−10.7	−4.9	−9.0	−7.3	−3.3	30

[a] Metals found in stainless steel (SUS303); [b] values reported per mole of the reactant metal.

Sizes of metal powders before and after milling

Table S9. Diameters *D* of metal particles before and after milling

Metal	before milling	after milling
	D (μm)	D (μm)
Al	138 ± 30.4	0.6 ± 0.3
Ti	30 ± 11	1.2 ± 0.4
Zn	3.9 ± 1.6	0.5 ± 0.2
Fe	76 ± 35	0.6 ± 0.5
Mn	6 ± 2	0.3 ± 0.1
Sn	12 ± 8	0.5 ± 0.2

Table S10. TiO, Ti_2O_3, and TiO_2 parameters

Parameters	TiO	Ti_2O_3	TiO_2
Particle radius R_1 ($\times 10^{-5}$ cm)	1.6[a)]	2.0[a)]	0.07[a)]
Density ρ_1 (g cm^{-3})	4.88[b)]	4.54[b)]	4.15[b)]
Poisson's ratio ν_1	0.26[b)]	0.32[b)]	0.27[b)]
Young's modulus e_1 ($\times 10^{10}$ dyn cm^{-2})	294[b)]	232[b)]	280[b)]
Vickers hardness (GPa)	14.2[b)]	6.3[b)]	12.1[b)]

[a)] Average of the radii distribution shown in Fig. S18 for each oxide; [b)] Calculated values obtained from ref. 41. Since it was not possible to obtain experimental values for TiO and Ti_2O_3, calculated values are listed. Values for TiO_2 from the same literature source are also listed to allow comparison with the calculated values for the other titanium oxides.

References

1. O. Tetens, *Z. Geophys.*, 1930, **6**, 297–309.
2. F. Xiao, R. Yang and Z. Liu, *Int. J. Hydrogen Energy*, 2022, **47**, 365–386.
3. S. Xu, X. Zhao and J. Liu, *Renew. Sustain. Energy Rev.*, 2018, **92***,* 17–37 (2018).
4. M. Esmaily, J.E. Svensson, S. Fajardo, N. Birbilis, G.S. Frankel, S. Virtanen, R. Arrabal, S. Thomas and L.G. Johansson, *Prog. Mater. Sci.*, 2017, **89***,* 92–193.
5. H.Z. Wang, D.Y.C. Leung, M.K.H. Leung and M. Ni, A review on hydrogen production using aluminum and aluminum alloys. *Renew. Sustain. Energy Rev.*, 2009, **13**, 845–853.
6. X. Huang, T. Gao, X. Pan, D. Wei, C. Lv, L. Qin, Y. Huang, A review: feasibility of hydrogen generation from the reaction between aluminum and water for fuel cell applications. *J. Power Sources*, 2013, **229**, 133–140.
7. M. Digne, P. Sautet, P. Raybaud, H. Toulhoat and E. Artacho, Structure and stability of aluminum hydroxides: a theoretical study. *J. Phys. Chem. B*, 2002, **106**, 5155–5162.
8. I. Vishnevetsky and M. Epstein, Production of hydrogen from solar zinc in steam atmosphere. *Int. J. Hydrogen Energy*, 2007, **32**, 2791–2802.
9. A. Steinfeld, A. Solar thermochemical production of hydrogen—a review. *Sol. Energy*, 2005, **78***,* 603–615.
10. A. Xu, Y. Bhawe and M.E. Davis, Low-temperature, manganese oxide-based, thermochemical water splitting cycle. *Proc. Natl. Acad. Sci. U.S.A.*, 2012, **109**, 9260–9264.
11. S. Dutta, S. Review on solar hydrogen: its prospects and limitations. *Energy Fuels*, 2021, **35**, 11613–11639.
12. T. Nakamura, Hydrogen production from water utilizing solar heat at high temperatures. *Sol. Energy*, 1977, **19**, 467–475.
13. J.D. Lee, *Concise Inorganic Chemistry*, 5th Edition (Chapman & Hall, 1999**)**.
14. R.L. Rich, *Inorganic Reactions in Water* (Springer, 2007).
15. Y. Yavor, S. Goroshin, J.M. Bergthorson and D.L. Frost, Comparative reactivity of industrial metal powders with water for hydrogen production. *Int. J. Hydrogen Energy*, 2015, **40**, 1026–1036.
16. P. Charvin, S. Abanades, F. Lemort and G. Flamant, Hydrogen production by three-step solar thermochemical cycles using hydroxides and metal oxide systems. *Energy Fuels*, 2007, **21**, 2919–2928.

17. Y. Mao, Y. Gao, W. Dong, H. Wu, Z. Song, X. Zhao, J. Sun and W. Wang, Hydrogen production via a two-step water splitting thermochemical cycle based on metal oxide – A review. *Appl. Energy*, 2020, **267**, 114860.
18. P. Charvin, S. Abanades, F. Lemont and G. Flamant, Experimental study of SnO_2/SnO/Sn thermochemical systems for solar production of hydrogen. *AIChE J.*, 2008, **54**, 2759–2767.
19. J. Zheng, D. Yang, W. Li, H. Fu and X. Li, Promoting H_2 generation from the reaction of Mg nanoparticles and water using cations. *Chem. Commun. (Camb.)*, 2013, **49**, 9437–9439.
20. I.V. Ikonitskii, N.A. Buzina, L.K. Kurnosova and E.N. Kropacheva, IR spectroscopic study of the reaction of titanium tetrachloride with some oxygen-containing compounds. *J. Appl. Spectrosc.*, 1981*,* **34**, 438–441.
21. W.B. Person, W.B. II Maier, Absolute integrated intensities of the infrared absorption bands of $TiCl_4$. *J. Chem. Phys*., 1978, **69**, 297–299.
22. S.P. Gupta, H.H. Nishad, S.D. Chakane, S.W. Gosavi, D.J. Late, P.S. Walke, Phase transformation in tungsten oxide nanoplates as a function of post-annealing temperature and its electrochemical influence on energy storage. *Nanoscale Adv.*, 2020, **2**, 4689–4701.
23. M.F. Daniel, B. Desbat, J.C. Lassegues, B. Gerand and M. Figlarz, Infrared and Raman study of WO_3 tungsten trioxides and WO_3, xH_2O tungsten trioxide tydrates. *J. Solid State Chem.*, 1987, **67**, 235–247.
24. F.K. Urakaev and V.V. Boldyrev, Mechanism and kinetics of mechanochemical processes in comminuting devices: 1. Theory. *Powder Technol*., 2000, **107**, 93–107.
25. F.K. Urakaev, Chapter 2 in *High-Energy Ball Milling: Mechanochemical Processing of Nanopowders*, 1st Edition, Ed: M. Sopicka-Lizer (Woodhead Publishing, 2010), pp. 9–44.
26. T. Mizutani, H. Ohta, T. Ueda, T. Kashiwagi, T. Fukuda, T. Shiobara and K. Saitow, Mechanochemically tailored silicon particles for efficient H_2 production: entropy and enthalpy engineering. *ACS Sustain. Chem. Eng*., 2023, **11**, 11769–11780.
27. P. Atkins and J. de Paula, *Physical Chemistry*, 10th Edition (Oxford University Press, 2014).
28. A.J. Bard, R. Parsons and J. Jordan, *Standard Potentials in Aqueous Solution* (CRC Press, 1985).
29. G.M. Barrow, *Physical Chemistry*, 6th Edition (McGraw Hill, 1996).
30. D.D. Wagman, W.H. Evans, V.B. Parker, R.H. Schumm, I. Halow, S.M. Bailey, K.L. Churney and R.L. Nuttall, The NBS tables of chemical thermodynamic properties.

Selected values for inorganic and C_1 and C_2 organic substances in SI units. *J. Phys. Chem. Ref. Data*, 1989, **18**, 1807–1812.

31. J.A. Dean, *Lange's Handbook of Chemistry*, 12th Edition (McGraw Hill, 1979).
32. L.V. Gurvich, I.V. Veits and C.B. Alcock, *Thermodynamic Properties of Individual Substances. Volumes 1 and 2*, 4th Edition (Hemisphere, 1989, 1991).
33. J.F. Shackelford and W. Alexander, *CRC Materials Science and Engineering Handbook*, 3rd Edition (CRC Press, 2001).
34. E.A. Brandes and G.B. Brook, *Smithells Metals Reference Book*, 7th Edition (Butterworth-Heinemann, 1992).
35. Y.S. Touloukian, R.W. Powell, C.Y. Ho and P.G. Klemens, *Thermophysical Properties of Matter – The TPRC Data Series. Volume 2. Thermal Conductivity - Nonmetallic Solids* (IFI/Plenum, 1971).
36. S.J. Smith, R. Stevens, S. Liu, G. Li, A. Navrotsky, J. Boerio-Goates and B.F. Woodfield, *Am. Mineral.*, 2009, **94**, 236.
37. P.D. Miller and J.W. Holladay, *Wear*, 1958, **2**, 133–140.
38. M. Sasaki, I. Nakamura, I. Takano and Y. Sawada, *Electr. Eng. Jpn.*, 2004, **149**, 1–7 (2004).
39. R. Hultgren, P.D. Desai, D.T. Hawkins, M. Gleiser, K.K. Kelley and D.D. Wagman, *Selected Values of the Thermodynamic Properties of the Elements* (American Society for Metals, 1973).
40. D.R. Stull and H. Prophet, *JANAF Thermochemical Tables* 2nd ed. (NSRDS-NBS-37, U.S. Department of Commence, 1971).
41. S.L. Tang, Y.F. Li, Y.R. Wang, Y.M. Gao, Q.L. Zheng and D.W. Yi, *Mater. Chem. Phys.*, 2018, **213**, 538–547.